SSCL-Preprint-9 (Rev. A)

SSCL-Preprint-9 (Rev. A)

Superconducting Super Collider Laboratory

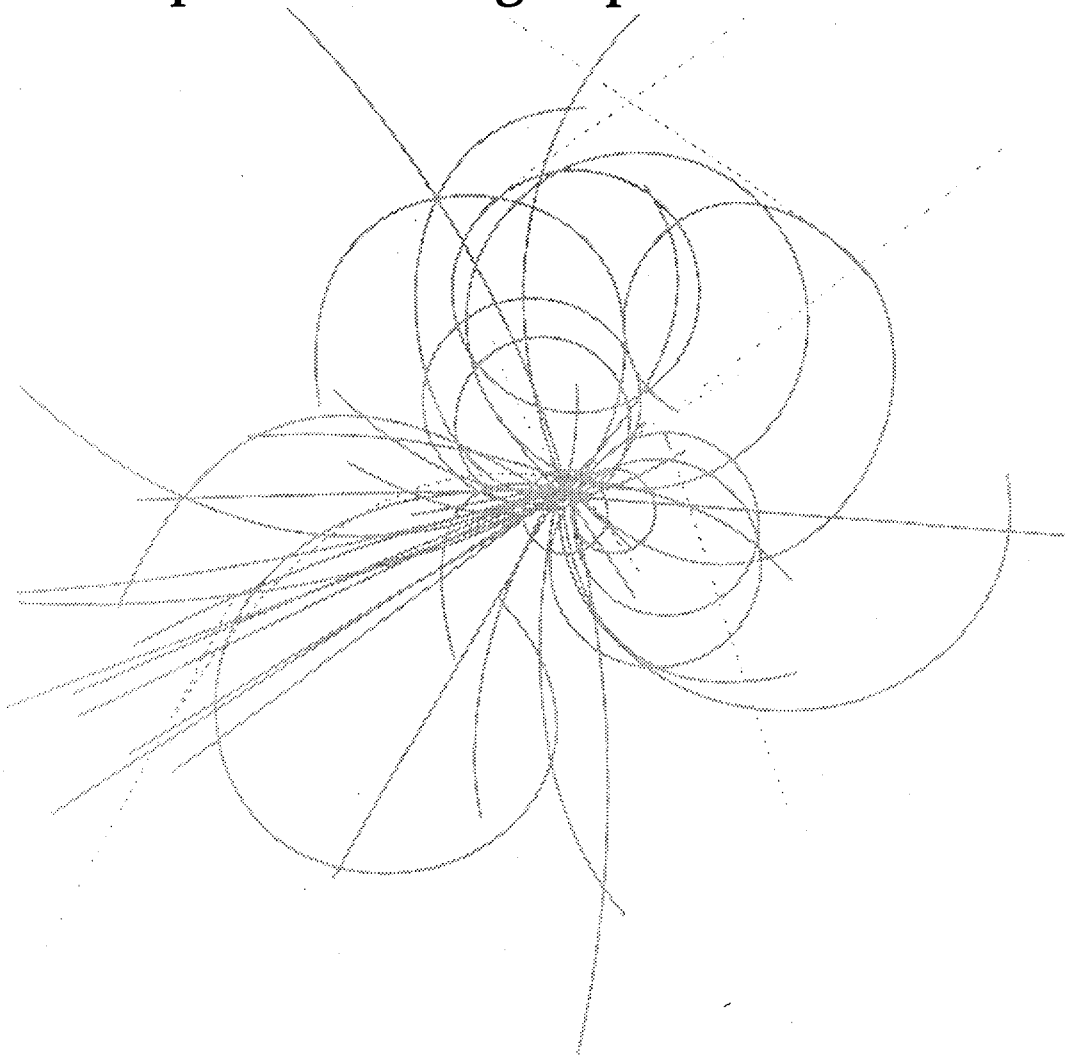

Instabilities in Beam Control Feedback Loops in Proton Synchrotrons

L. K. Mestha, C. M. Kwan, and K. S. Yeung

October 1992

SSCL-Preprint-9 (Rev. A)

Instabilities in Beam Control Feedback Loops in Proton Synchrotrons*

L. K. Mestha,[1] C. M. Kwan,[2] and K. S. Yeung[2]

Superconducting Super Collider Laboratory†
2550 Beckleymeade Avenue
Dallas, TX 75237

October 1992

* Submitted to *Particle Accelerators.*

[1] Superconducting Super Collider Laboratory, Dallas, Texas.

[2] The University of Texas, Arlington, Texas 76019.

† Operated by the Universities Research Association, Inc., for the U.S. Department of Energy under Contract No. DE-AC35-89ER40486.

Copyright information to be inserted by the Publishers

INSTABILITIES IN BEAM CONTROL FEEDBACK LOOPS IN PROTON SYNCHROTRONS

L. K. MESTHA

Accelerator Systems Division
*Superconducting Super Collider Laboratory,*Dallas, Texas 75237*

C. M. KWAN and K. S. YEUNG

University of Texas, Arlington, Texas 76019

A generalized beam control model is derived in terms of accelerator parameters. Using this model, stability conditions are derived for several loop configurations with and without a synchronization loop in the feedback system in the absence of beam-loading effects. A new synchronization scheme analyzed in this paper enables phase-locking of the reference bunch in the lower-energy machine with a reference bucket in the higher-energy machine with controlled phase slippage when ideal phase values are suitably adjusted for transfer. The mathematical technique used here greatly enhances the stability analysis for fast-cycling machines. Analogy with commonly used frequency domain techniques is shown with some examples. Limits under model approximations are presented. Detailed derivations are shown for the configuration planned for the Low Energy Booster of the Superconducting Super Collider. Only the results are tabulated for other loop configurations. The approach indicates explicitly how the time-varying gains can be designed for fast-cycling machines. In cases where the derivative of the synchronous phase and the momentum error are large, the method shows how to obtain a suitable compensation.

1 INTRODUCTION

There are two important parameters—the magnetic field and the accelerating voltage—associated with beam control. Since the magnetic field system is designed to bend and focus the beam, it has a long time constant. Hence all the beam control feedback loops are concentrated at the radio frequency (rf) accelerating system. The rf accelerating cavities are driven by programmed amplitude and frequency function. An rf power amplifier drives the cavity, and a high voltage appears on the gap. The amplitude of this voltage is programmed and is controlled by each cavity-local feedback loop.[1] The frequency function is generated globally to all the cavities. To control the beam in the synchrotron there may be six different

* Operated by Universities Research Association, Inc., for the U.S. Department of Energy under Contract No. DE-AC35-89ER40486.

primary feedback loops interacting with the beam at a given time. Three loops are local to the rf cavity: high-bandwidth cavity phase and amplitude loops used to minimize the effects due to beam loading, and a low-bandwidth cavity tuning loop. The loops global to the ring accelerating system are a radial loop to keep the beam on orbit, a beam phase loop to damp the dipole synchrotron oscillations, and a synchronization loop to essentially lock with the succeeding machine for beam transfer.

There are several ways these loops are designed using classical techniques.[2] The loop design approach adopted by many authors assumes an incomplete beam model, especially for fast-cycling machines with resonant magnetic field, since in such cases the time variation in accelerating frequency places greater demands on the loop stability. We therefore have developed a generalized time-domain control model. The model will allow us to analyze and design different hardware-intensive feedback strategies from the viewpoint of beam dynamics. Due to the complexity of the model and the stability analysis of the loops that follows, we have divided the studies into two parts. The first part is related to the global loops by assuming that the local cavity loops are fast compared to the global loops; hence this part will be applicable to low-intensity proton synchrotrons. The second part covers the studies with the cavity model, including the effects due to beam loading and cavity tuning. The results of the second part will be published elsewhere.

The generalized control model was developed from a particle tracking model. The derivation of the particle tracking model is shown in Reference 3. We then apply the simple linear state feedback concept and obtain instability boundaries for different loop configurations with and without the synchronization loop throughout acceleration. Linear, time-varying state feedback techniques are used since the control problem is multi-state. We also show the analogy with the frequency domain results whenever necessary. We use a new synchronization loop[4] to phase-lock the two accelerators, which enables us to close the loop from any point during the accelerating cycle. When the synchronization loop is not in place, conceptually the loop configurations are those being used in various machines around the world. Improvement to the existing loops is suggested due to the time-varying nature of the accelerating system. Wherever possible, we have attempted to derive mathematical expressions for the instability boundaries in terms of the rf and lattice parameters. A detailed derivation of the stability chart for the loop gains is shown for the configuration planned for controlling the Low Energy Booster (LEB) of the Superconducting Super Collider. The charts will help to avoid the unstable region during acceleration, thereby preventing unwanted longitudinal oscillations of the beam. Also, for operation of machines below and above transition, the signs of the loops become extremely important, as can be clearly seen from the diagrams. Especially when the synchronization loop is closed very early on during the cycle, the signs of the loop gain are not apparent, but they are clear from the equations of the instability boundary shown in this paper. To make the chart applicable for many types of practical implementations, we introduce the concept of moving the imaginary axis by a certain amount towards the left half of the s-plane.

2 FEEDBACK CONTROL MODEL

For the purpose of designing feedback controllers to control the beam due to both magnetic and electric field errors, the tracking model shown in Reference 3 is not sufficient. The longitudinal dynamics of the beam contained in this model must be extracted in differential-equation form by identifying suitable control inputs such as (1) frequency and phase of the signal driving the rf cavities, and (2) the machine parameters to be controlled. In general, the controllable parameters with global rf feedback are the (1) coherent dipole beam oscillations, (2) radial orbit deviation from the mean orbit, and (3) the synchronizing phase with the higher-energy machine. Before discussing the derivation of the model, it will be useful to know the planned loop configuration for the LEB.

The global low-power rf signal driving the cavities is generated by a single frequency source, namely a Direct Digital Synthesizer (DDS) as shown by the schematic diagram in Fig. 1. The frequency and phase of the rf signal are controlled by feedback loops from the beam to the frequency source and by a global phase shifter. The local phase shifters are passive and are required only to phase the rf signal going to each cavity due to the geometrical spacing between the cavities. By varying the frequency and phase of the rf signal, the voltage seen by the beam and hence the energy can be varied. The deviation in the orbital position is measured with horizontal electrodes at the beam position monitor and is corrected by varying the phase of the rf signal in the global phase shifter. This loop, called the "radial loop," generally has slow time response and is not able to damp "coherent dipole oscillations" in the beam due to field errors. The coherent oscillations are the motion connected with the bunch, whereas the incoherent oscillations are motion of the individual particle inside the bunch. Therefore a "beam phase loop" is included to the frequency source. In this loop the beam signal is compared directly from a wall current monitor with the rf signal in a beam phase detector. It is compared to the synchronous phase of the beam, and an error signal is obtained. The error signal is proportional to the dipole oscillations in the beam. The beam phase error is converted to appropriate frequency shift through a feedback controller. The frequency shift is added to the programmed frequency curve at the input end of the DDS.

With only radial and phase loops, the beam will circulate around the ring without proper synchronization of a given bunch with the stable bucket in the Medium Energy Booster (MEB). The synchronization is required for filling batches of LEB bunches into the MEB for collider operation. The configuration of the synchronization loop shown in Fig. 1 provides the means to phase-lock the reference beam bunch in the LEB to the reference bucket in the MEB. In this approach a Time to Digital Converter (TDC) is used to measure the position of the designated LEB reference bunch for each MEB revolution. The time-of-flight information is multiplied by a stored velocity profile for the synchronous particle. By comparing these values with the ideal phase values for the designated LEB reference bunch for each MEB revolution, an error signal is generated. The error signal is converted to frequency shift from the controller, which is then added to the ideal frequency program. Thus

the LEB reference bunch is phase-locked to the ideal phase values stored in the computer. This enables phase-locking of the bunch with controlled phase slippage when ideal phase values are suitably adjusted for transfer. As is well known, the difficulty lies mainly in studying the stability of feedback loops with all three loops in operation. The loop configuration shown in Fig. 1 is not unique, and it is difficult to know whether this is an optimum approach without analyzing the loops together. Other possible configurations include the radial loop to the input end of the DDS or to the global voltage function. Also, the synchronization loop can be connected to the phase shifter. By knowing the stability region for a given configuration we would be able to decide on the best approach for the accelerator. A good control model will help in this regard. We describe the derivation of the model by first discussing the synchronization scheme in detail.

2.1 The Synchronization Model

For extraction purposes the phase of the lower-energy machine must be adjusted to match the phase of the higher-energy machine. The higher-energy machine will be coasting with no acceleration at the time the lower-energy machine is accelerated. In the literature one sees two schemes[5,6] for achieving synchronous transfer of the beam: phase-locking and phase-slippage. In the phase-locking scheme, at a known time before injection to the next accelerator the phase and frequency of the accelerating machine are locked to the extraction frequency. In accelerator jargon the process of synchronization is known as "cogging." For low-energy accelerators with a long flat-top region, there is generally enough time available for cogging. But for resonant field machines, the time is limited because the magnetic field does not remain at the flat top for a long time. Also, since the time required to phase-lock the two machines depends on the slip factor, η, which is a function of the lattice parameters, it would be difficult to maneuver the beam with large energy excursions close to the flat top. Also, locking in advance with a variable frequency machine becomes difficult due to large phase accumulation. Alternatively, it has been a tradition in that type of machine to use the phase-slippage scheme without using any active feedback. In this scheme, the frequency of the accelerating machine is offset a few cycles relative to the extraction frequency at a pre-determined time before transfer. As a result, the phase of the accelerating frequency slips relative to the fixed frequency. Consequently, several phase coincidence points of the reference wave occur at a beat frequency equal to the offset frequency. One of these points is used to trigger the synchronous transfer of the beam.

Two techniques for synchronization mentioned above do not provide a means to transfer by selecting a particular bunch as the first bunch in the higher-energy machine. A more general approach for synchronization is to consider the locking of the phase of the variable-frequency source with the phase of the fixed-frequency source throughout or anytime during the acceleration of the lower-energy machine with active feedback. In this scheme we can choose a reference bunch in the lower-energy machine and force it to follow a pre-programmed "trip-plan" so that at the instant of transfer it will have the same energy and phase as the higher-energy

reference wave. The trip-plan has at least one point at flat B-field region where the machines have exact phase for the purpose of synchronous beam transfer. We have been successful in testing the scheme with two oscillators for the LEB frequency profile. We were able to lock the oscillators for the complete LEB acceleration cycle. The implementation technique used in the "proof of principle" test is discussed in Reference 4. The trip-plan approach affords all the benefits of existing schemes and also, by choosing the appropriate control strategy, enables us to keep track of the gap in the lower-energy machine.

As indicated above in the trip-plan approach, the reference bunch of the lower-energy machine is tracked with respect to a designated empty bucket of the higher-energy machine. The empty bucket is the destination point for the reference bunch of the lower-energy machine. Let $\tilde{t}_k^s$ be the time covered by the ideal reference bunch in the higher-energy machine for kth turn in the lower-energy machine. The lower-energy machines are small in circumference compared to the higher-energy machine; hence for the machines with non-integer circumference ratios, at flat top, after the reference bunch in the higher-energy machine has crossed the reference point, the reference bunch in the lower-energy machine takes a certain time to cross the marker. During one turn of the reference bunch in the higher-energy machine, the lower-energy machine reference bunch may have circled several turns depending on the path covered by the reference bunch and the speed at that time. A general scenario is shown in Fig. 2. If t_k^s is the time when the reference bunch in the lower-energy machine reaches the reference point in the kth turn, then the trip-plan is given by

$$(S_k)_{trip-plan} = v_k^s \left(t_k^s - \tilde{t}_k^s\right). \tag{2.1}$$

The subscript k indicates the turn number, and the superscript s indicates the parameter used for a synchronous particle throughout this paper. Hence, v_k^s represents the velocity of the synchronous particle for kth turn. The trip-plan is plotted for the LEB and MEB synchronization in Fig. 3. For synchronous transfer, the synchronizing phase is equal to zero (ignoring the transfer line delays). The MEB to LEB circumference ratio is $3960/570 = 6.9473684$, which means that when the frequencies are the same at the end of one MEB turn, the LEB reference bunch would have completed six full turns and a semi-turn. By adding this semi-turn 19 times, we get one full LEB turn. Hence, there will be 19 MEB turns before the LEB reference bunch reaches the same reference point again. This is clearly visible in the trip-plan in Fig. 3.

The trip-plan calculated by Eq. (2.1) is for an ideal synchronous particle. In the presence of field errors, the actual path covered by the reference bunch is different and can be referred to as "trip." Ignoring the errors in the higher-energy machine, and with the beam assumed to be coasting at fixed frequency, the trip for kth turn of the lower-energy machine is given by

$$(S_k)_{actual} = \left(v_k^s + \delta v_k\right)\left(t_k - \tilde{t}_k^s\right), \tag{2.2}$$

where δv_k is the change in velocity from that of the synchronous particle and t_k is the actual traversal time of the lower-energy machine. The actual traversal time of

the lower-energy machine reference bunch is different from t_k^s used in Eq. (2.1) due to field errors. It can be modeled by adding up the total traversal time required by the actual particle up to k turns as follows:

$$t_k = t_k^s - \sum_{n=1}^{k} \delta\tau_n, \tag{2.3}$$

where $\delta\tau_k$ is the deviation with respect to the time taken by the synchronous particle in the lower-energy machine. The negative sign appears because in the machine operating below transition a particle with too much energy travels on a circle with greater radius, but since it is faster it takes less time to return to the gap than the ideal particle. By subtracting Eq. (2.1) from Eq. (2.2), the error in synchronizing phase can be obtained for kth turn as follows:

$$\delta S_k = -v_k^s \left(1 + \frac{\delta v_k}{v_k^s}\right) \sum_{n=1}^{k} \delta\tau_n + \left\{ \frac{\delta v_k}{v_k^s} (S_k)_{trip-plan} \right\} + \delta S_0. \tag{2.4}$$

To lock the two reference bunches, we need to reduce the synchronization phase to zero. δS_0 is the phase error we have deliberately created by selecting a given reference bunch in the lower-energy machine that may be several meters away from trip-plan. The deviation in the actual velocity of the bunch is generally small. That is, the ratio $(\delta v_k)/v_k^s$ is small if we choose enough samples in the trip-plan. Hence, terms within the flower brackets can be ignored. Eq. (2.4) is in difference-equation form, which can be converted to differential-equation form by introducing τ^s as the traversal time of the ideal synchronous particle. While transforming to continuous domain, the summation term is replaced by the integral. Hence, the synchronization phase error is written as

$$\delta S \cong -v^s \int \frac{\delta\tau}{\tau^s} dt + \delta S_0. \tag{2.5}$$

The synchronization model will be useful if we express in terms of the radial orbit shift and the dipole field error. Substituting for $\frac{\delta\tau}{\tau^s}$ from Reference 3, the following equation can be obtained:

$$\delta S = -v^s \int \left[\eta^s \gamma_T^2 \frac{\delta R}{R^s} - \frac{1}{(\gamma^s)^2} \frac{\delta B}{B^s} \right] dt + \delta S_0, \tag{2.6}$$

where $\eta^s = \left(\frac{1}{\gamma_T^2}\right) - \left(\frac{1}{(\gamma^s)^2}\right)$ is the slip factor for a synchronous particle.

When the field error is zero, the synchronization phase error is due to the orbital deviation. The relationship between the phase error and orbital deviation is weighted by the slip factor. If we have synchronized the reference bunch in the low-energy machine to the trip-plan earlier in the cycle, then smaller slip factor would be beneficial. It means the particle tries to stay on orbit. This is quite the opposite of the requirement for the existing synchronization schemes, such as phase-locking and phase-slippage schemes.

2.2 *Transverse Orbital Deviation*

The mean orbital deviation is zero for an ideal synchronous particle. In the presence of field errors, it is not zero. A general model is required to describe the longitudinal dynamics associated with the orbital deviations. For a given turn in the low-energy machine, the dynamics are well described by the particle tracking model shown in Reference 3. However, to obtain a differential equation with appropriate control in the presence of errors, we need to use the energy equation shown in Reference 7. If $\overline{\Delta E}$ is the difference between the energy of the synchronous particle and the particle we are tracking, then

$$\overline{\Delta E}_{k+1} = \overline{\Delta E}_k + \Big(e(V_k^s + \delta V_k)\sin\phi_k - eV_k^s \sin(\phi_k^s)\Big), \tag{2.7}$$

where δV_k is given by

$$\delta V_k = \delta V_k^c + \delta V_k^e, \tag{2.8}$$

with δV_k^c the control supplied to the cavity gap voltage, δV_k^e the error in the cavity voltage for kth turn, and ϕ_k^s the particle phase for the ideal synchronous case. The quantity δV_k^c can be set to zero when we do not use global amplitude feedback. The energy equation is in finite difference form. It can be transformed to a differential equation in the usual way, as follows:

$$\frac{d\delta E}{dt} = \frac{eV^s\beta^s c}{2\pi R^s}\left[\left(1 + \frac{\delta V^c}{V^s} + \frac{\delta V^e}{V^s}\right)\sin(\phi) - \sin(\phi^s)\right]. \tag{2.9}$$

The particle phase, ϕ, can be written in terms of the nominal synchronous phase, ϕ^s; of the deviation from the synchronous phase representing the synchrotron oscillations, $\delta\phi^s$; of the systematic phase error, $\tilde{\phi}^e$; and also of a small phase shift, $\delta\phi^c$, as supplied by the controller. That is,

$$\phi = \phi^s + \delta\phi^c + \delta\phi^s + \tilde{\phi}^e. \tag{2.10}$$

The phase shift $\delta\phi^c$ is included as a control input, since the radial loop can be connected to the global phase shifter after the frequency source, as in the case of Fermilab Booster low-level rf system[8,9] (also see Fig. 1). From Reference 7 it is well known that

$$\delta E = (\beta^s)^2 \frac{\delta P}{P^s} E^s. \tag{2.11}$$

The momentum change can be expressed in terms of the radial position change and the field change.[3] Hence by taking the first derivative of Eq. (2.11), we can express the rate of energy change in terms of the radial position change and field change by the following equation:

$$\frac{d\delta E}{dt} = \dot{A}_1\delta R + A_1\frac{d\delta R}{dt} + A_2\frac{d\delta B}{dt} + \dot{A}_2\delta B, \tag{2.12}$$

where the coefficients $\dot{A}_1$ and $\dot{A}_2$ are the first derivatives of A_1 and A_2 and are given by

$$A_1 = \frac{(\beta^s)^2\gamma_T^2 E^s}{R^s} \qquad \text{and} \qquad A_2 = \frac{(\beta^s)^2 E^s}{B^s}. \tag{2.13}$$

Comparing Eqs. (2.12) and (2.9) and rewriting the resulting equation, we obtain the desired equation for the radial orbital deviations:

$$\frac{d\delta R}{dt} = \frac{A_3}{A_1}\left[\left(1 + \frac{\delta V^c}{V^s} + \frac{\delta V^e}{V^s}\right)\sin(\phi) - \sin(\phi^s)\right] - \frac{\dot{A}_1}{A_1}\delta R - \frac{A_2}{A_1}\delta\dot{B} - \frac{\dot{A}_2}{A_1}\delta B, \quad (2.14)$$

where A_3 is the time-varying coefficient given by

$$A_3 = \frac{eV^s\beta^s c}{2\pi R^s}. \quad (2.15)$$

Eq. (2.14) combined with Eq. (2.10) describes the dynamics of the orbital deviation.

2.3 The Particle Phase Model

For control purposes, the longitudinal dynamics described by Eq. (2.14) are incomplete without representing the synchrotron oscillations in terms of the controllable and measurable parameters. The particle phase has synchrotron oscillations whenever we are tracking an off-momentum particle. The momentum offset could be due to field error. If f_k^s is the nominal frequency as programmed in the oscillator, δf_k^c is the control input generated by the controller, and δf_k^e is the error in the oscillator itself, then the beam phase equation can be written as

$$\phi_{k+1} = \phi_k + 2\pi(f_k^s + \delta f_k^c + \delta f_k^e)(\tau_k^s + \delta\tau_k). \quad (2.16)$$

$\delta\tau_k$ can be expressed in terms of radial orbit shift and dipole field error, as was done in Eq. (2.6).

$$\frac{\phi_{k+1} - \phi_k}{\tau_k^s} = 2\pi(f_k^s + \delta f_k^c + \delta f_k^e)\left[1 + \eta_k^s\gamma_T^2\frac{\delta R_k}{R^s} - \frac{1}{(\gamma_k^s)^2}\frac{\delta B_k}{B_k^s}\right]. \quad (2.17)$$

Eq. (2.17) can be written in the differential-equation form by ignoring the second-order terms as follows:

$$\frac{d\phi}{dt} = \frac{2\pi f^s\eta\gamma_T^2}{R^s}\delta R - \frac{2\pi f^s}{(\gamma^s)^2 B^s}\delta B + 2\pi f^s + 2\pi\delta f^c + 2\pi\delta f^e. \quad (2.18)$$

The term $2\pi f^s$ can be ignored because it is multiples of 360°. By substituting from Eq. (2.10) for the particle phase, we obtain the following differential equation for the synchrotron oscillations:

$$\frac{d\delta\phi^s}{dt} = \frac{2\pi f^s\eta\gamma_T^2}{R^s}\delta R + 2\pi\delta f^c - \frac{d\delta\phi^c}{dt} - \frac{2\pi f^s}{(\gamma^s)^2 B^s}\delta B + 2\pi\delta f^e - \frac{d\phi_0^s}{dt} + \frac{\beta^s c\phi^e}{2\pi R^s}, \quad (2.19)$$

where ϕ^e is the change in systematic phase error per turn. In most machines, depending on the electronics used, this type of error would not be large. Eqs. (2.6), (2.14), and (2.19) are compared with the tracking code of Reference 3 for the expected values of the errors and the control inputs. The simulated results agree very closely with the tracking code for the LEB parameters.

3 STATE SPACE MODEL

The main reason for generating an accurate beam model with errors was to analyze the loops using well-known state-feedback techniques. Application of the state-variable techniques to the rf beam control has advantages over the conventional transfer function approach. The state-feedback technique permits the analysis of systems with rapidly changing parameters, as in fast-cycling synchrotrons. All the internal modes of excitation are visible, whereas with the transfer function approach, they tend not to appear because of the pole-zero cancellation with the numerator and the denominator. Hence, in this section we convert the beam control model to state-variable form.

The model shown in the main text can be written in state space form by assuming the following definition for the measured quantities and the control inputs:

$$\begin{aligned} x_1 &= \delta S \qquad u = \delta f^c \\ x_2 &= \delta R \qquad w = \delta V^c/V^s. \\ x_3 &= \delta\phi^s \\ x_4 &= \delta\phi^c \end{aligned} \tag{3.1}$$

In the above equation δS, δR, and $\delta\phi^s$ are measured quantities, whereas $\delta\phi^c$ is a control input used to shift the phase of the global rf signal. Also, in our beam model the global frequency shift and the amplitude shift are represented by control inputs. The field shift, δB, cannot be considered like this, since we are not feeding any signal to the magnet system power supply from the global beam control system. Now, by using the new variables in Eq. (2.6) we obtain the state space description for the synchronization model as follows:

$$\dot{x}_1 = a_{11}x_1 + a_{12}x_2 + d_{11}\delta B - a_{11}x_0, \tag{3.2}$$

where the time-varying coefficients are shown in Tab. 1. Similarly, the state space description of the radial orbit shift can be obtained by substituting Eq. (3.1) in Eq. (2.14). After simplifying the algebra and rearranging the coefficients, we get the following non-linear equation:

$$\begin{aligned} \dot{x}_2 &= a_{22}x_2 + (a_{23} - \tilde{a}_{23}\omega)\sin(x_3 + x_4) + (a_{24} - \tilde{a}_{24}\omega)\cos(x_3 + x_4) \\ &\quad + \tilde{a}_{24} + d_{21}\delta B + \tilde{d}_{21}\delta\dot{B}, \end{aligned} \tag{3.3}$$

where the time-varying coefficients are again listed in Tab. 1. The state space description of the phase oscillations is given by substituting Eq. (3.1) in Eq. (2.19). Thus,

$$\begin{aligned} \dot{x}_3 &= a_{32}x_2 + b_{31}u + v - \dot{\phi}^s + d_{31}\delta B + b_{31}\delta f^e + d_{32}\phi^e \\ \dot{x}_4 &= -v. \end{aligned} \tag{3.4}$$

Eqs. (3.2) and (3.4) are linear and time-varying. For synchrotrons such as the Super Collider, the time variation can be ignored. Eq. (3.3) is non-linear in nature, but

is linearizable for a small range of operation in x_3 and x_4. Linear control methods can be applied to the simplified model.

4 LINEAR STATE FEEDBACK CONTROLLER

It is generally easy to design a linear controller for a time-varying system. Linear state feedback techniques are attractive when all the states are measurable. To simplify the complexity further, we will ignore the global amplitude feedback loop from any of the states x_1, x_2, x_3, and x_4. At the end of this paper we show the design by including the global amplitude loop. Hence ω is considered zero. By ignoring errors, the straightforward linear model of the system can be written as follows in matrix form:

$$\begin{bmatrix} \dot{x}_1 \\ \dot{x}_2 \\ \dot{x}_3 \\ \dot{x}_4 \end{bmatrix} = \begin{bmatrix} a_{11} & a_{12} & 0 & 0 \\ 0 & a_{22} & a_{23} & a_{23} \\ 0 & a_{32} & 0 & 0 \\ 0 & 0 & 0 & 0 \end{bmatrix} \begin{bmatrix} x_1 \\ x_2 \\ x_3 \\ x_4 \end{bmatrix} + \begin{bmatrix} b_{31} & 1 \\ 0 & -1 \end{bmatrix} \begin{bmatrix} u \\ v \end{bmatrix}^{-\dot{\phi}^s + d_{32}\phi^e} \tag{4.1}$$

Eq. (4.1) is a linearized open loop control model for time-varying machine such as the LEB. For a time-invariant machine such as the Super Collider, the coefficients a_{11} and a_{22} are zero. In standard vector form Eq. (4.1) can be written as

$$\dot{\underline{x}} = \underline{A}\,\underline{x} + \underline{B}\,\underline{u}, \tag{4.2}$$

where $\underline{x}$ represents the state vector, $\underline{A}$ represents the system matrix, $\underline{B}$ represents the input matrix, and $\underline{u}$ represents the control vector. Eq. (4.2) is known as a state-differential equation. In Tab. 1 all the state equations are summarized, including the general open loop linear control model.

Clearly the system matrix $\underline{A}$ is singular. This means the open loop system is unstable. It is true that if we do not have feedback and if there is δR error, then the locking to the trip-plan is not perfect. The feedback of the state variables with appropriate gain vector will stabilize the loops. For the configuration shown in Fig. 1, the following state feedback law can be applied:

$$\begin{aligned} u &= -k_1 x_1 - k_3 x_3 - u^e \\ v &= -k_2 x_2 - k_4 x_4, \end{aligned} \tag{4.3}$$

where $u^e = (d_{32}\phi^e - \dot{\phi}^s)/2\pi$. With the above feedback strategy the loop diagram of Fig. 1 is rewritten in Fig. 4. The term $\dot{\phi}^s - d_{32}\phi^e/2\pi$ is added with u in Eq. (4.3) for the time-varying machines such as the LEB, to cancel out $\dot{\phi}^s$ and ϕ^e appearing in the system Eq. (4.1). From the simulation results with the tracking code of Reference 3 an improvement in the loop performance is seen due to the nullification of these terms. The phase shift, $\delta\phi^c$, is derived by integrating v from Eq. (4.3). It is interesting to note in the feedback strategy that k_4 is deliberately chosen to be non-zero. The reason for this will be clear when we look at the closed loop system

matrix obtained by substituting Eq. (4.3) in Eq. (4.1):

$$\begin{bmatrix} \dot{x}_1 \\ \dot{x}_2 \\ \dot{x}_3 \\ \dot{x}_4 \end{bmatrix} = \begin{bmatrix} a_{11} & a_{12} & 0 & 0 \\ 0 & a_{22} & a_{23} & a_{23} \\ -k_1 b_{31} & a_{32} - k_2 & -k_3 b_{31} & -k_4 \\ 0 & k_2 & 0 & k_4 \end{bmatrix} \begin{bmatrix} x_1 \\ x_2 \\ x_3 \\ x_4 \end{bmatrix}$$

$$\Rightarrow \qquad \dot{\underline{x}} = \underline{A}_{cl}\underline{x}. \tag{4.4}$$

The closed loop system matrix, $\underline{A}_{cl}$, is non-singular. However, we still do not know the stability bounds on the system. It can be obtained by applying the following stability theorem:

For a system to be globally asymptotically stable (see stability theorem in Reference 10), these conditions must be met: all the eigen values of $\underline{A}_{cl}(t)$ have negative real parts, the matrix, $\underline{A}_{cl}(t)$, remains bounded, and the following integral is finite:

$$\int_0^\infty \underline{A}_{cl}^T(t)\underline{A}_{cl}(t)dt < \infty. \tag{4.5}$$

Solving Eq. (4.4) for eigen values is complicated. Hence, an alternative approach is to obtain a closed loop characteristic equation by taking the Laplace Transform of Eq. (4.4) at a given time in the acceleration cycle and applying Ruth-Hurwitz (RH) criteria. Still, for global asymptotic stability the matrix, $\underline{A}_{cl}(t)$, must remain bounded and the integral shown in Eq. (4.5) must be satisfied as long as the beam stays within the machine. Analogy with the currently used radial loops is clearly visible when we substitute the equation for v from Eq. (4.3) in the state equation for $\dot{x}_4$ in Eq. (3.4), since the ratio

$$\frac{X_4(s)}{X_2(s)} = \frac{k_2}{s - k_4} \tag{4.6}$$

is a single-pole filter and is the transfer function used in the radial loop. By choosing appropriate negative values of k_2 and k_4, the gain and corner frequency of the filter can be fixed. The phase shift, x_4, is obtained from the following equation:

$$x_4 = \int (k_2 x_2 + k_4 x_4)dt. \tag{4.7}$$

As a second example, say for a two-pole filter in the radial loop in place of a single-pole filter, v can be chosen as follows:

$$v = -k_2 \int x_2 dt - k_4 \int x_4 dt - k_5 x_4. \tag{4.8}$$

In writing Eq. (4.8), the time variation in the gains, k_2, k_4, and k_5 is ignored. The transfer function of the filter is then equal to

$$\frac{X_4(s)}{X_2(s)} = \frac{k_2}{s^2 - k_5 s - k_4}. \tag{4.9}$$

By choosing the magnitude and signs of the gains k_2, k_4, and k_5, the stability of the system can be analyzed. When u is used as in Eq. (4.3) and v as in Eq. (4.8), the closed loop system matrix becomes sixth order. However, for the sake of simplicity we have examined the case with only a single-pole transfer function.

To obtain the characteristic equation of the closed loop matrix we proceed as follows. First take the Laplace Transform of Eq. (4.4) at a given time in the cycle and generate a characteristic matrix, which is given by:

$$s\underline{I} - \underline{A}_{cl} = \begin{bmatrix} s - a_{11} & -a_{12} & 0 & 0 \\ 0 & s - a_{22} & -a_{23} & -a_{23} \\ k_1 b_{31} & -(a_{32} - k_2) & s + k_1 b_{31} & k_4 \\ 0 & -k_2 & 0 & s - k_4 \end{bmatrix}, \tag{4.10}$$

where $\underline{I}$ is the identity matrix. From the characteristic matrix it is clear that for a time-invariant machine (which could be the case even when the beam is just coasting), if k_4 is zero, then the system will show a pole at the origin. This means the loops are marginally stable. For the LEB, when we approach the top energy the change in the beam velocity is small, meaning $a_{11} \approx 0$. Hence the stability of the loops cannot be guaranteed. This justifies the use of a non-zero k_4 for the configuration of Fig. 1. For stability analysis, as we discussed earlier, we generate a characteristic equation from the matrix of Eq. 4.10, then apply RH criteria. The 4th-order characteristic equation of the characteristic matrix is

$$s^4 + a_3 s^3 + a_2 s^2 + a_1 s + a_0 = 0. \tag{4.11}$$

The coefficients of the characteristic equation are written in terms of the loop gains and the machine parameters as follows:

$$\begin{aligned} a_3 &= k_3 b_{31} - k_4 - (a_{11} + a_{22}) \\ a_2 &= -(k_3 k_4 b_{31} + a_{32} a_{23}) + a_{11} a_{22} - (k_3 b_{31} - k_4)(a_{11} + a_{22}) \\ a_1 &= a_{23} a_{32} k_4 - a_{23} b_{31} k_2 k_3 + a_{12} a_{23} b_{31} k_1 + a_{11} a_{23} a_{32} \\ &\quad + a_{22} a_{11} (k_3 b_{31} - k_4) + (a_{11} + a_{22}) b_{31} k_3 k_4 \\ a_0 &= -a_{12} a_{23} b_{31} k_1 k_4 - a_{11} (a_{23} a_{32} k_4 + \tilde{a}_{22} b_{31} k_3 k_4 - a_{23} b_{31} k_2 k_3). \end{aligned} \tag{4.12}$$

By applying RH criteria we obtain the following four inequalities for stability:

$$\begin{aligned} &\text{(i)} \quad (a_3 a_2 - a_1) a_1 - a_3^2 a_0 > 0 \\ &\text{(ii)} \quad (a_3 a_2 - a_1) > 0 \\ &\text{(iii)} \quad a_3 > 0 \\ &\text{(iv)} \quad a_0 > 0. \end{aligned} \tag{4.13}$$

Conditions shown in Eqs. (4.13) are critical for the loops to remain stable throughout acceleration. It is, however, unclear from the inequalities alone what the limits are on the gains for the loops to remain stable at all times. Hence the conditions can be further explored to obtain meaningful information by plotting the trajectories of the stability boundaries. At first we do the analysis by ignoring a_{11} and a_{22}, for simplicity. This is done below.

5 INSTABILITY BOUNDARIES

Boundaries for the loop instability can be calculated by equating equations obtained from RH criteria to zero. Since there are four gains in the loop, it becomes difficult to imagine a 4th-dimensional stability boundary. Hence, we can further simplify the problem to a two-dimensional case by first fixing k_3 and k_4 to satisfy the inequality $a_3 > 0$ in Eq. (4.13), then plotting the boundaries for k_2 versus k_1 from the remaining inequalities. To plot the boundaries we proceed as follows:

Condition (i): Equating the left-hand side of the inequality (i) in Eq. (4.13) to zero, we obtain the contour for marginal stability:

$$(a_3 a_2 - a_1)a_1 - a_3^2 a_0 = 0. \tag{5.1}$$

Now by substituting the coefficients shown in Eq. (4.12) into Eq. (5.1), the contour can be expressed in k_1 and k_2 space:

$$k_1^2 + 2Mk_1k_2 + M^2k_2^2 + Dk_1 + Ek_2 + F = 0, \tag{5.2}$$

with

$$\begin{aligned} M &= \frac{R^s k_3}{v^s \eta^s \gamma_T^2} \\ D &= a[-1 + \xi k_4^2] \\ E &= Ma[-1 + 2\pi\xi k_3 k_4] \\ F &= \frac{\tilde{C} f^s k_4}{v^s}. \end{aligned} \tag{5.3}$$

The variables a, ξ, and $\tilde{C}$ are

$$\begin{aligned} a &= \left(\frac{2\pi k_3 + k_4}{v^s}\right) f^s \\ \xi &= \frac{hR^s}{2\pi f^s c\nu^2}\left(\frac{2\pi k_3 - k_4}{2\pi k_3 + k_4}\right) \\ \tilde{C} &= \frac{2\pi k_3 f^s}{v^s} - \frac{hR^s k_3}{v^s c\nu^2}(2\pi k_3 - k_4)k_4, \end{aligned} \tag{5.4}$$

where ν is the synchrotron tune equal to

$$\nu = \sqrt{\frac{-h\eta^s eV^s \cos(\phi^s)}{2\pi\beta^s E^s}}.$$

Eq. (5.2) is in a generalized, second-degree form. We can show from the formulas of plane analytic geometry that this equation is a parabola since it satisfies all the conditions for the parabola.[11] But the parabola is tilted (since the coefficient of the product k_1k_2 is not zero), with the coordinate axes k_1 and k_2 with an angle α given

by

$$\tan 2\alpha = \frac{2M}{1-M^2}. \tag{5.5}$$

Hence we need to perform coordinate transformation. The transformation formulas are given by

$$\begin{aligned} k_1 &= \bar{k}_1 \cos\alpha - \bar{k}_2 \sin\alpha = (\bar{k}_1 - M\bar{k}_2)/\sqrt{1+M^2} \\ k_2 &= \bar{k}_1 \sin\alpha + \bar{k}_2 \cos\alpha = (M\bar{k}_1 + \bar{k}_2)/\sqrt{1+M^2}. \end{aligned} \tag{5.6}$$

Substituting Eq. (5.6) into Eq. (5.2), we obtain the equation for the parabola:

$$\bar{k}_2 = P\bar{k}_1^2 + Q\bar{k}_1 + R, \tag{5.7}$$

where the coefficients are given by

$$\begin{aligned} P &= \frac{(1+M^2)^{3/2} v^s}{-M\xi k_4(2\pi k_3 - k_4)(2\pi k_3 + k_4) f^s} \\ Q &= \frac{1 + M^2 + \xi k_4(2\pi k_3 M^2 - k_4)}{M\xi k_4(2\pi k_3 - k_4)} \\ R &= \frac{-\tilde{C}}{M\xi(2\pi k_3 - k_4)(2\pi k_3 + k_4)}. \end{aligned} \tag{5.8}$$

The coefficients P, Q, and R of the parabola can be further simplified by choosing the ratio $k_4/k_3 \ll 1$. Also, the time constant of the beam phase loop can be chosen approximately equal to $1/k_3$. For the LEB a value of $k_3 = 3000$ is chosen. If a time constant of 1/4 of the synchrotron period is needed, then k_3 must be chosen to be approximately 100,000, because one shortest synchrotron period is approximately $40\mu s$. Even then, M is less than 1. With such a choice of k_3, the factor M in Eq. (5.3) is far less than 1. So, the coefficients of the tilted parabola can be reduced to

$$P = -\mu\frac{(v^s)^2}{2\pi k_3^3 k_4}, \quad Q = \mu\frac{v^s f^s}{k_3^2 k_4}, \quad R = -\mu\frac{(f^s)^2}{k_3^2}, \quad \text{and} \quad \mu = \frac{\eta^s \gamma_T^2 c\nu^2}{h(R^s)^2}. \tag{5.9}$$

The vertex of the parabola $(\bar{k}_{1v}, \bar{k}_{2v})$ in the new coordinate system is given by

$$\bar{k}_{1v} = \frac{\pi f^s k_3}{v^s}, \qquad \bar{k}_{2v} = \frac{\mu(f^s)^2(\pi k_3 - 2k_4)}{2k_3^2 k_4}. \tag{5.10}$$

The parabola is plotted in Fig. 5 for the LEB parameters at 1 ms from the injection, with $k_3 = 3000$ and $k_4 = -20$. The vertex of the parabola is in the first quadrant, and it is concave down. The stable region, as required by the RH criteria, inequality (i) in Eq. (4.13), is inside the parabola. Note that if k_4 is chosen positive, the parabola becomes concave up, with the vertex in the fourth quadrant. The stable region will again be inside the parabola. The parabola intersects the $\bar{k}_1$ axis at two points. The left lobe intersects at the origin, and the right lobe intersects at $(2\pi f^s k_3/v^s, 0)$. For smaller gains, k_3, the x-coordinate of the vertex

moves closer to the origin. Also the y-coordinate of the vertex increases, and the point of intersection of the right lobe moves closer, tending to cause the parabola to become more focussed. This reduces the upper limit on the synchronization loop gain. Conversely, the larger the gain k_3, the more spread out the parabola is.

Condition (ii): By substituting Eqs. (4.12) in the RH criteria, inequality (ii) of Eq. (4.13), then equating the results to zero, the second contour for marginal stability can be obtained:

$$k_1 + Mk_2 = \tilde{C}. \tag{5.11}$$

Now by applying coordinate transformation, i.e., by using Eq. (5.6) in Eq. (5.11), we obtain the following equation for the straight line:

$$\bar{k}_1 = \frac{\tilde{C}}{\sqrt{1+M^2}}. \tag{5.12}$$

For the LEB, Eq. (5.12) can be reduced to

$$\bar{k}_1 = \frac{2\pi f^s k_3}{v^s}. \tag{5.13}$$

This instability line is parallel to the $\bar{k}_2$ axis and intersects the $\bar{k}_1$ axis at $2\pi f^s k_3/v^s$, which is the same point where the right lobe of the parabola intersects with the $\bar{k}_1$ axis. The region on the left side of this line satisfies RH criteria, inequality (ii) of Eq. (4.13), for stability and hence is a stable region as shown by the dotted lines in Fig. 5.

Condition (iii): In this case, $2\pi k_3$ is selected to be greater than k_4 for stability.

Condition (iv): From the RH criteria, inequality (iv) of Eq. (4.13), for stability we note the product $k_1 k_4 < 0$ for machines operating below transition. The stability boundary can be obtained by equating the product $k_1 k_4$ to zero, then transforming the identity to a new coordinate system by using Eqs. (5.6). After transformation, the equality is given by

$$\bar{k}_1 - M\bar{k}_2 = 0. \tag{5.14}$$

The stability region depends on the sign of k_4 and is shown in Figs. 6(a) and 6(b) for the LEB, which includes a region common to the three inequalities, (i), (ii), and (iv). The contour enclosing the shaded area is the instability boundary in $\bar{k}_1$, $\bar{k}_2$ space for $k_4 < 0$ and $k_4 > 0$. The real values of the gain can be obtained from the transformation formulae shown in Eqs. (5.5) and (5.6). We have to watch out for the sign of the radial loop depending on the other loop gains.

As we stated earlier, for the loops to remain stable the inequalities shown in Eq. (4.13) must be satisfied along with the condition that the integral shown in Eq. (4.5) is finite. By evaluating the definite integral for the duration of the accelerating period, say for the LEB, we see that the integral reaches a finite value. In the stability analysis discussed so far with the synchronization loop operating along with the beam phase loop and the radial loop, we have ignored the time-varying

terms, a_{11} and a_{22}. We included these terms and plotted the parabola at different times during the acceleration cycle for the LEB. The $\bar{k}_2$ axis coordinate of the vertex reduces in magnitude without significant change in the $\bar{k}_1$ axis coordinate of the vertex. The angle of tilt, α, of the parabola turned out to be very significant; this will be discussed later with additional stability diagrams at a different time during the cycle. However, the terms a_{11} and a_{22} did not have a major effect on the instability boundaries. On the other hand, the approximations used in deriving the state space model from the finite-difference equations combined with the sampling effects in the feedback loops cause considerable changes to the stability trajectories. To make the chart applicable for many types of practical implementations, we introduce the concept of moving the imaginary axis by a certain amount toward the left half of the s-plane. This effectively restricts the guaranteed stable region to a small area in $\bar{k}_1$, $\bar{k}_2$ space. The details are shown below.

6 STABILITY LIMITS DUE TO MODEL APPROXIMATIONS

The beam control model shown in Tab. 1 is a result of the approximation we introduced while converting the discrete equations to continuous form. With the continuous model, the closed loop stability analysis obviously becomes simple, but when applied to the real accelerator the performance will be somewhat different. On the other hand, the application of linear discrete theory using the discrete model for loop stability may be complicated, since the traversal time of the macroparticle is modulated over the accelerating cycle, leading to irregular sampling. Furthermore, if the feedback loops are implemented digitally, the sampling period enhances the stability problems. Hence, we show a technique below to use the stability diagram discussed earlier for most of the practical implementations. The technique is discussed by taking the example of the LEB.

Fig. 7 is plotted to portray the location of the roots of the characteristic Eq. (4.11): λ_1, λ_2, λ_3, and λ_4 for the loop gains $k_1 = 25$, $k_2 = 5000$, $k_3 = 3000$, and $k_4 = -20$. Roots λ_1 and λ_2 are very close to the imaginary axis; the closed loop system response is dominated by the root closest to the imaginary axis, since the time response of the mode with the root λ_1 decays very slowly compared to the mode with the root λ_4. Also, since two eigen values are closer to the imaginary axis when compared to λ_3 and λ_4, they may be in the marginal stability region due to model approximations for the choice of the loop gains, k_1, k_2, k_3, and k_4, even though these gains satisfy the stability bounds shown in Fig. 6. Another way to learn the stability bounds is by moving the imaginary axis of Fig. 7 left by an amount ϵ and redrawing the stability contours. By selecting the gains to fall within the new contours, we can guarantee that the loops remain stable. The value of ϵ can be chosen by trial and error; this is purely intuitive. By partitioning λ_4 into subintervals, we can choose ϵ to be equal to one of them. In this way we are ensuring that the eigen values within the ϵ boundary obtained with gains k_1, k_2, k_3, and k_4, indicate the marginal stability. This method, however, does not overcome the effects due to unmodeled dynamics in the system. Now the new s-parameter, $\bar{s}$, can be defined

as

$$\bar{s} = s - \epsilon. \tag{6.1}$$

Substituting for s from Eq. (6.1) in Eq. (4.11), a new characteristic equation is obtained:

$$\bar{s}^4 + \bar{a}_3\bar{s}^3 + \bar{a}_2\bar{s}^2 + \bar{a}_1\bar{s} + \bar{a}_0 = 0, \tag{6.2}$$

where the new coefficients are given by

$$\begin{aligned} \bar{a}_3 &= a_3 + 4\epsilon \\ \bar{a}_2 &= a_2 + 3\epsilon(a_3 + 2\epsilon) \\ \bar{a}_1 &= a_1 + \epsilon(2a_2 + 3\epsilon a_3 + 4\epsilon^2) \\ \bar{a}_0 &= a_0 + \epsilon(a_1 + \epsilon a_2 + \epsilon^2 a_3 + \epsilon^3). \end{aligned} \tag{6.3}$$

By applying RH criteria, we obtain the new inequalities for stability:

$$\begin{aligned} &\text{(i)} \quad (\bar{a}_3\bar{a}_2 - \bar{a}_1)\bar{a}_1 - \bar{a}_3^2\bar{a}_0 > 0 \\ &\text{(ii)} \quad (\bar{a}_3\bar{a}_2 - \bar{a}_1) > 0 \\ &\text{(iii)} \quad \bar{a}_3 > 0 \\ &\text{(iv)} \quad \bar{a}_0 > 0. \end{aligned} \tag{6.4}$$

By equating the left-hand side of the inequalities (i), (ii), and (iv) to zero, new contours of the instability boundary for different values of ϵ are obtained. The new coefficients of the parabola can be obtained by following the procedure described in Section 5 above. Hence we do not show the expressions of the coefficients of the new parabola. Notice that the new parabola (with ϵ and the parameters a_{11} and a_{22} included) also has the tilt angle, α, described by Eq. (5.5). Therefore, the contours of the new stability region are shown in Fig. 8 by performing the coordinate transformation using Eq. (5.6) for the LEB at 1 ms, 20 ms, and 49 ms for $k_3 = 3000$, $k_4 = -20$, and an ϵ value of -150. Clearly, the common stability region is reduced as acceleration proceeds due to model approximation.

On most occasions it is likely that the synchronization loop is not closed at the beginning of the acceleration cycle, unless there is a requirement to synchronize a particular bunch as the first bunch in the higher-energy machine. When the synchronization loop is not closed, the beam phase loop and the radial loop will be operating. Loop gains have to be designed based on a new stability limit. Hence an analysis of the loop stability is done below for operations without the synchronization loop for the configuration of Fig. 1. Also, there are several alternative feedback configurations possible, and it is difficult to know which approach is a good one. Hence we evaluate most of the commonly known loop configurations by following the procedure outlined above. We then discuss the stability diagrams for each of them.

7 STABILITY OF LOOPS WITH ALTERNATIVE FEEDBACK STRUCTURES

In this section we obtain the stability diagrams for beam control loops with several possible structures with and without the synchronization loop in place. The

procedure is very similar to the studies shown above. Tabs. 2 through 7 show the feedback structures and the inequalities for stability for a time-varying machine with the shifted imaginary axis. Also, the contours are obtained as simple equations when ϵ, a_{11}, and a_{22} are ignored. Salient points are highlighted on the diagram. The "adder circuits" in the following sections are used to indicate the summing node before the DDS.

Beam Phase Loop to the Adder Circuits, and Radial Loop to the Phase Shifter

The inequalities for this configuration are shown in Tab. 2. The marginal stability contours obtained by equating the left-hand side of the inequalities (i) and (iii) to zero are hyperbolae when $a_{22} \neq 0$ and $\epsilon \neq 0$. But when a_{22} and ϵ are ignored, all three conditions describe straight lines, $k_2 = a_{32}$, $k_2 = 0$, and $k_3 = 0$. In Fig. 9(a) stability conditions are shown for the LEB at 1 ms for $\epsilon = 0$. Since a_{22} is not completely zero, we see the hyperbola from condition (i) with asymptotes at $k_2 = a_{32}$ and $k_3 = 0$. Condition (iii) is also a hyperbola, but it is almost coincident with the $k_2 = 0$ axis due to the size of the scale. The shaded area in the k_2–k_3 space is in the second quadrant, which indicates the stability region for the loops. Since the line $k_2 = a_{32}$ (the asymptote of the hyperbola for condition (i)), is proportional to the product, $f^s\eta^s$, we see that the region of stability will contract as acceleration proceeds. The instability boundaries for ϵ values of -150 are shown in Fig. 9(b) at 49 ms. The closed contour enclosing the shaded area has considerably contracted when compared with the area at 1 ms. If the gains k_2 and k_3 are selected to lie in the shaded area at 49 ms for the LEB, the loop stability can be guaranteed. With such a choice, the difficulty of arranging the hardware to vary the radial loop gain with time can be prevented. Of course, the time variation u^e (see Tab. 1) is required in the beam phase loop for machines like the LEB. For machines operating above transition, the stability region will fall in the first quadrant of the k_2–k_3 space as indicated by the asymptote $k_2 = a_{32}$. If there is transition crossing in the middle of the cycle, the sign of the radial loop gain must be changed.

Beam Phase Loop, Radial Loop, and Synchronization Loop to the Adder Circuits

This type of configuration seems to offer a large stability region with capability to synchronize a selected reference bunch with the higher-energy machine. In Tab. 3 the loop equations are shown with the instability boundaries for an ideal situation. Fig. 10(a) is plotted to show the stability region in the k_1–k_2 space when the beam phase loop gain is fixed at 3000. The intersection of the line represented by condition (i) with the $k_2 = 0$ axis is linearly dependent on the loop gain of the beam phase loop and the rf frequency-to-velocity ratio. Because of the time dependency, the stable region is confined to one quadrant only. In Fig. 10(b) the stability region is shown with model approximations when $\epsilon = -150$. Condition (iii) is acting in such a way that the common stable region between 1 ms and 49 ms is reduced.

Beam Phase Loop and Radial Loop to the Adder Circuits

The stability diagram and the related inequalities are shown in Fig. 11 and Tab. 4, respectively. The point of intersection of the lines $k_2 = \eta^s\gamma_T^2 f^s/R^s$ and $k_3 = 0$ is

a salient point in this diagram. The radial loop gain k_2 is required to be varied with time, since the salient point moves toward the origin in the k_2–k_3 space. For $\epsilon = -150$, curves do not demonstrate an observable difference. When the configuration shown in Tab. 4 is used in conjunction with Tab. 3 for synchronization, a high-gain capability is possible.

Beam Phase Loop to the Adder Circuits, Radial Loop and Synchronization Loops to the Phase Shifters

In this scheme the synchronization loop is connected to the phase shifter as shown in Tab. 5. The instability boundaries consist of a parabola and two straight lines, as in Figs. 12(a), 12(b), and 12(c), at 1 ms, 20 ms, and 49 ms, respectively. The stable region is well spread out in the k_1–k_2 space at 1 ms and 20 ms. However, at 49 ms there seems to be no clear region available for stability when $\epsilon = -150$. This means that the instability in the loop would start growing somewhere close to the end of the acceleration cycle if the beam phase loop gain is not decreased substantially. Alternately, if k_3 is decreased progressively, then the k_1 coordinate of the vertex of the parabola moves further left, as shown in Fig. 12(d). This figure is drawn for the case with $k_3 = 1000$, a factor of 3 less than in Figs. 12(a) through 12(c). The straight line representing condition (ii) becomes more negative, expanding the stable region. Thus an additional time variation in the beam phase loop is required to have sufficient stability region.

Beam Phase Loop and Synchronization Loop to the Adder Circuits, and Radial Loop to the Global Amplitude

Instead of connecting the radial loop to the adder circuits or to the phase shifter, one can also insert it to modulate the cavity voltage, as shown in the configuration of Tab. 6. In this case the stability boundaries differ from the other configurations. As shown in Fig. 13, the common stability region during the whole acceleration cycle is narrow at 30 ms, which coincides with the point where the synchronous phase angle is maximum. Effectively, it turns out that the radial loop gain must vary in time unless the phase loop gain is reduced substantially at the maximum phase angle point to increase the stability region shown by the shaded area in the k_1–k_2 space.

Beam Phase Loop to the Adder Circuits and Radial Loop to the Global Amplitude

When the synchronization loop is removed from the configuration of Tab. 6, the loop stability region is as shown in Fig. 14. The boundary equations are presented in Tab. 7. Variation in the beam phase loop gain may not be required if k_2 is selected to be very high.

Other loop configurations, such as the beam phase loop and the radial loop to the phase shifter, are inherently unstable and are not discussed.

8 SIMULATION RESULTS

Simulation studies are carried out for the configuration described above. We present the results for Fig. 1 in the presence of errors. Sources of errors in the beam control loops are many, and they depend on the type of implementation. Usual source of errors are (1) field errors (cavity voltage and magnetic field), (2) errors in the measurement of radial position, (3) systematic and random errors in the beam phase measurement, (4) errors in the frequency source due to the stability limits on oscillators, (5) errors in calculating the trip-plan, (6) errors while ramping the programmed frequency, and (7) systematic error in the global phase shifter. Descriptions of these errors are shown in Reference 12.

The decay of the states x_1, x_2, x_3, and x_4 are shown in Figs. 15(a) through 15(d) for feedback configuration of Fig. 1, with and without systematic errors. The change in systematic errors in the global phase shifter and the beam phase loop do not appear to give synchronism if the synchronization loop is closed early on in the cycle unless the error is known accurately. Whereas, the constant systematic error does not seem to affect synchronization. In Fig. 15(e) the control input is also shown. The particle we tracked was 30 m away from the reference point at $t = 0$. We chose the sampling interval of 1 MEB turn (which is equal to 13.249 μs—hence the cable delays can be ignored). The tracking model we chose was in finite-difference form, as shown in Reference 3. The steady state errors in x_1 and x_2 are derived in Appendix A. When there is no systematic error in the bending field, the steady state error in synchronization is $\beta^s c\phi^e/(2\pi)^2 k_1 R^s$, which clearly depends on the gain of the synchronization loop. If we know ϕ^e in advance, we can compensate for it by including the time-varying gain in the phase loop, as shown by Eq. (4.3). Another useful piece of information to note is the radial position at the time of transfer; this is equal to $R^s \delta B/(\gamma^s)^2 \gamma_T^2 \eta^s B^s$ (Eq. (A.8)), which is independent of ϕ^e. Also, since the bunch contains several particles we need to know whether the particle with a maximum initial phase offset could be tracked into the same bucket. Fig. 15(f) shows the difference in phase of the offset particle with the synchronous phase. This information is useful in determining whether there is any particle loss. The initial offset with respect to rf signal was $\pm 165°$, receiving the same control input as shown in Fig. 15(e). Particles over 165° did not remain in the same bucket.

It appears that the random errors do not give problems in synchronization when the loop is closed very early on during acceleration. The systematic error, however, is going to be a problem unless it is decoupled by adding linear or non-linear dynamics in the closed loop system or by recalculating the trip-plan by trial-and-error or by increasing the synchronization loop gain. The stability regions we have predicted in several figures above are confirmed through simulation using the tracking code of Reference 3. Also, the choice is to have a large stability region for the gains and to provide time variation throughout acceleration whenever necessary. In the analogue implementation of the beam phase loop, ϕ^e is not usually subtracted from the output of the beam phase detector of Fig. 1; instead a filter is used to dc-couple the synchronous phase. No doubt, analogue and digital implementation both perform the same function, but for the case when the synchrotron frequency falls

within the cutoff frequency of the filter, the stability margins of the loops change. Hence a better way to implement is to subtract ϕ^s digitally from the digitized phase information.

9 CONCLUSIONS

In this paper we describe the application of modern linear state feedback techniques for analyzing the stability of rf beam control feedback loops. Since the state feedback concept is in time-domain, it is particularly useful for fast-cycling accelerators where the rf frequency is changing rapidly with time. Terms such as the derivative of the synchronous phase and systematic errors are found to be important and must be suitably compensated either in the beam phase loop or in the radial loop. A novel method of phase-locking a reference bunch in the lower-energy machine with a stable bucket in the higher-energy machine is analyzed without disabling the other feedback loops.

A generalized beam control model is derived from a single-particle tracking model, giving a good insight into the time-varying nature of the control problem for fast-cycling machines. The generalized model enlarged the class of loop configurations that can be treated in detail. The stability limits were expressed in terms of the machine parameters for quick reference. A new technique is introduced to obtain the limits in the presence of model approximations, since such approximations tend to reduce the stability margin. Diagrams shown in this paper give a clear understanding of the signs of the loop gains for machine operation below and above transition; this is especially useful when the synchronization loop is closed. For some loop configurations, time-varying gains are essential and are apparent from the boundary equations. With the synchronization loop closed, although the loops are stable, systematic errors will not give the desired synchronism of the reference bunch unless they are decoupled. If for some reason such decoupling is not possible, then non-linear robustifying loops are required. The design of a type of such loops is described in Reference 12. At the end the stability limits were confirmed using the particle-tracking model in finite-difference form. Since the beam control loops were studied by ignoring beam-loading effects on rf cavities, the stability diagrams are accurate when the local cavity loops are fast compared to global loops.

ACKNOWLEDGEMENTS

The authors wish to thank Bob Webber for continuing discussions and encouragement.

REFERENCES

1. L. K. Mestha, "Beam Control Feedback Loops for the Low Energy Booster," SSCL-559, Superconducting Super Collider Laboratory, Dallas, Texas, 1991.

2. D. Boussard, "Design of a Ring RF System," CERN Accelerator School Proceedings, CERN 91-04, Geneva, May 1991.
3. L. K. Mestha, "Particle Tracking Code for Simulating Global RF Feedback," SSCL-506, Superconducting Super Collider Laboratory, Dallas, Texas, 1992.
4. L. K. Mestha, "Phase-Locked Loop with Controlled Phase Slippage," U.S. Patent Application, DOE Case No. S-74,282.
5. Y. Kimura, T. Kawakubo, K. Takata, and T. Kamei, "Synchronous transfer of beam from the booster to the main ring in the KEK proton synchrotron," *IEEE Transactions on Nuclear Science*, Vol. NS-**24**, No. 3, June 1977.
6. S. R. Koscielniak, "RF System Aspects of Longitudinal Beam Control," TRIUMF Design Note, TRI-DN-91-K183, Vancouver, Canada, August 1991.
7. D. A. Edwards and M. J. Syphers, "An Introduction to the Physics of Particle Accelerators," SSC Laboratory Publication, Dallas, Texas, 1990.
8. C. Kerns, J. Crisp, Q. Kerns, and H. Miller, "New Low-Level RF System for the Fermilab Booster Synchrotron," Particle Accelerator Conference, Washington, D.C., March 16–19, 1987.
9. R. C. Webber and L. K. Mestha, "Proposal to Test a New Low Level RF System on the Fermi National Accelerator Laboratory Booster Synchrotron," SSCL Controlled Document, ADA-3120001, November 1991.
10. J. J. E. Slotine and W. Li, *Applied Nonlinear Control*, (Prentice Hall, New Jersey, 1990).
11. M. Vygodsky, *Mathematical Handbook*, MIR Publishers, Moscow, 1978.
12. L. K. Mestha, C. M. Kwan, and K. S. Yeung, "Stabilization of Global Beam Control Feedback Loops for SSC Low Energy Booster Using Sliding-Mode Controller," SSCL Preprint-15, December 1991.

APPENDIX A: STEADY STATE ERROR CALCULATION

The steady state error in the states x_1, x_2, and x_3 are attributable to the systematic errors in the magnetic field, δB, and the phase shift, ϕ^e. We show below how to calculate the steady state error for the configuration of Fig. 1. The same technique can be applied to other loop arrangements.

Consider the general state space model of Tab. 1, which can be rewritten in the following form:

$$\begin{bmatrix} \dot{x}_1 \\ \dot{x}_2 \\ \dot{x}_3 \\ \dot{x}_4 \end{bmatrix} = \begin{bmatrix} a_{11} & a_{12} & 0 & 0 \\ 0 & a_{22} & a_{23} & a_{23} \\ 0 & a_{32} & 0 & 0 \\ 0 & 0 & 0 & 0 \end{bmatrix} \begin{bmatrix} x_1 \\ x_2 \\ x_3 \\ x_4 \end{bmatrix} + \begin{bmatrix} 0 & 0 & 0 & 0 \\ 0 & -\tilde{a}_{24} & 0 & 0 \\ 0 & 0 & b_{31} & 1 \\ 0 & 0 & 0 & -1 \end{bmatrix} \begin{bmatrix} 0 \\ w \\ u \\ v \end{bmatrix} + \begin{bmatrix} d_{11} & 0 & 0 & 0 \\ 0 & d_{21} & 0 & 0 \\ 0 & d_{31} & d_{32} & 0 \\ 0 & 0 & 0 & 0 \end{bmatrix} \begin{bmatrix} \delta B \\ \delta B \\ \phi^e \\ 0 \end{bmatrix} - \dot{\phi}^s. \tag{A.1}$$

We consider no systematic error in the beam phase loop for simplicity. Now by substituting $u = -k_1 x_1 - k_3 x_3 + (\dot{\phi}^s/2\pi)$, $v = -k_2 x_2 - k_4 x_4$, and $w = 0$ in the

general equation Eq. (A.1), we obtain the following closed loop matrix equation:

$$\begin{bmatrix} \dot{x}_1 \\ \dot{x}_2 \\ \dot{x}_3 \\ \dot{x}_4 \end{bmatrix} = \begin{bmatrix} a_{11} & a_{12} & 0 & 0 \\ 0 & a_{22} & a_{23} & a_{23} \\ -k_1 b_{31} & a_{32} - k_2 & -k_3 b_{31} & -k_4 \\ 0 & k_2 & 0 & k_4 \end{bmatrix} \begin{bmatrix} x_1 \\ x_2 \\ x_3 \\ x_4 \end{bmatrix} + \begin{bmatrix} d_{11} & 0 & 0 & 0 \\ 0 & d_{21} & 0 & 0 \\ 0 & d_{31} & d_{32} & 0 \\ 0 & 0 & 0 & 0 \end{bmatrix} \begin{bmatrix} \delta B \\ \delta B \\ \phi^e \\ 0 \end{bmatrix}. \tag{A.2}$$

That is,

$$\dot{\underline{x}} = \underline{A}_{cl}\underline{x} + \underline{d}\,\underline{u}^e, \tag{A.3}$$

where $\underline{d}$ and $\underline{u}^e$ contribute to the error component. Taking Laplace Transform of Eq. (A.3), we obtain

$$\underline{x}(s) = \frac{\underline{d}\,\underline{u}^e}{s(s\underline{I} - \underline{A}_{cl})}. \tag{A.4}$$

The steady state values of the states x_1, x_2, x_3, and x_4 are calculated at 50 ms by designating the steady state condition on the state matrix as $\underline{x}_\infty$.

$$\therefore \qquad \underline{x}_\infty = \operatorname*{Limit}_{s \to 0} s\underline{x}(s). \tag{A.5}$$

Substituting Eq. (A.4) in Eq. (A.5), $\underline{x}_\infty$ is obtained:

$$\underline{x}_\infty = -\frac{\underline{d}\,\underline{u}^e}{\underline{A}_{cl}}. \tag{A.6}$$

Solving for x_1 and x_2 from Eq. (A.6), the following steady state values are obtained:

$$x_{1\infty} = \frac{d_{32}\phi^e}{b_{31}k_1} + \frac{\delta B}{b_{31}k_1}\left[\frac{(k_2 k_3 b_{31} - a_{32})d_{11}}{a_{12}k_4} + d_{31}\right] \tag{A.7}$$

and

$$x_{2\infty} = -\frac{R^s}{(\gamma^s)^2\gamma_T^2\eta^s}\,\frac{\delta B}{B^s}. \tag{A.8}$$

Clearly, from Eq. (A.7) we note that when there is no systematic error in the bending field, the synchronization phase error due only to the change in systematic error, ϕ^e, is

$$x_{1\infty} = \frac{\beta^s c\phi^e}{(2\pi)^2 k_1 R^s}. \tag{A.9}$$

By having a large loop gain in the synchronization loop, the steady state error can be reduced. Also, steady state error in the radial position does not depend on the radial loop gain, as seen by Eq. (A.8).

LIST OF PRINCIPAL SYMBOLS

$(\cdot)^s$: $(\cdot)$ Synchronous quantity

$(\cdot)^c$: $(\cdot)$ Control variable

$(\cdot)_k$: $(\cdot)$ Variable at the kth turn

$(\cdot)^e$: Error between actual quantity $(\cdot)$ and that of synchronous particle $(\cdot)^s$

$(\cdot)_0$: Initial value of the quantity $(\cdot)$

$\dot{(\cdot)}$: First derivative of quantity $(\cdot)$

$\delta(\cdot)$: Small variation in the quantity $(\cdot)$

TABLE 1: State space model.

Non-Linear State Space Model:

$$\dot{x}_1 = a_{11}x_1 + a_{12}x_2 + d_{11}\delta B - a_{11}x_0$$

$$\dot{x}_2 = a_{22}x_2 + (a_{23} - \tilde{a}_{23}\omega)\sin(x_3 + x_4) + (a_{24} - \tilde{a}_{24}\omega)\cos(x_3 + x_4) + \tilde{a}_{24} + d_{21}\delta B + \tilde{d}_{21}\delta\dot{B}$$

$$\dot{x}_3 = a_{32}x_2 + b_{31}u + v - \dot{\phi}^s + d_{31}\delta B + b_{31}\delta f^e + d_{32}\phi^e$$

$$\dot{x}_4 = -v$$

General Linear State Space Model:

$$\begin{bmatrix}\dot{x}_1\\ \dot{x}_2\\ \dot{x}_3\\ \dot{x}_4\end{bmatrix} = \begin{bmatrix}a_{11} & a_{12} & 0 & 0\\ 0 & a_{22} & a_{23} & a_{23}\\ 0 & a_{32} & 0 & 0\\ 0 & 0 & 0 & 0\end{bmatrix}\begin{bmatrix}x_1\\ x_2\\ x_3\\ x_4\end{bmatrix} + \begin{bmatrix}0 & 0 & 0 & 0\\ 0 & -\tilde{a}_{24} & 0 & 0\\ 0 & 0 & b_{31} & 1\\ 0 & 0 & 0 & -1\end{bmatrix}\begin{bmatrix}0\\ \omega\\ u\\ v\end{bmatrix} + b_{31}u^e$$

Coefficients:

$a_{11} = \frac{\dot{v}^s}{v^s}$	$\tilde{a}_{23} = -\frac{A_3}{A_1}\cos\phi^s$	$d_{11} = \frac{v^s}{(\gamma^s)^2 B^s}$
$a_{12} = -\frac{v^s\eta^s\gamma_T^2}{R^s}$	$a_{24} = \frac{A_3}{A_1}\left(1 + \frac{\delta V^e}{V^s}\right)\sin\phi^s$	$d_{21} = -\frac{\dot{A}_2}{A_1}$
$a_{22} = -\frac{\dot{A}_1}{A_1}$	$\tilde{a}_{24} = -\frac{A_3}{A_1}\sin\phi^s$	$\tilde{d}_{21} = -\frac{A_2}{A_1}$
$a_{23} = \frac{A_3}{A_1}\left(1 + \frac{\delta V^e}{V^s}\right)\cos\phi^s$	$a_{32} = \frac{2\pi f^s\eta^s\gamma_T^2}{R^s}$	$d_{31} = \frac{2\pi f^s}{(\gamma^s)^2 B^s}$
	$b_{31} = 2\pi$	$d_{32} = \frac{\beta^s c}{2\pi R^s}$
$A_1 = \frac{(\beta^s)^2\gamma_T^2 E^s}{R^s}$	$A_2 = \frac{(\beta^s)^2 E^s}{B^s}$	$A_3 = \frac{eV^s\beta^s c}{2\pi R^s}$

Variables:

$$x_0 = \delta S_0 \quad x_1 = \delta S \quad x_2 = \delta R \quad x_3 = \delta\phi^s \quad x_4 = \delta\phi^c \quad u = \delta f^c \quad \omega = \delta V^c/V^s$$

Errors: $\delta B \quad \delta f^e \quad \delta V^e \quad \phi^e \quad u^e = (d_{32}\phi^e - \dot{\phi}^s)/b_{31}$

TABLE 2: Loop equations.

Loop Diagram:

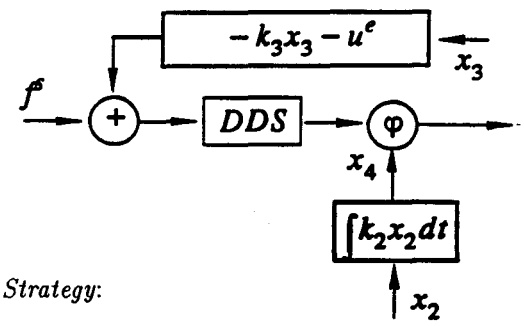

Feedback Strategy:

$u = -k_3x_3 - u^e$

$v = -k_2x_2$

Coefficients of the Characteristic Polynomial:

$\bar{a}_0 = a_0 + a_1\epsilon + a_2\epsilon^2 + \epsilon^3$ $\quad a_0 = -a_{23}b_{31}k_2k_3$

$\bar{a}_1 = a_1 + 2\epsilon a_2 + 3\epsilon^2$ and $a_1 = -(k_3b_{31}a_{22} + a_{23}a_{32})$

$\bar{a}_2 = a_2 + 3\epsilon$ $\quad a_2 = k_3b_{31} - a_{22}$

Stability Inequalities:

(i) $(\bar{a}_2\bar{a}_1 - \bar{a}_0) > 0$

(ii) $\bar{a}_2 > 0$

(iii) $\bar{a}_0 > 0$

Instability Boundaries for $\epsilon = 0$, $a_{22} = 0$:

$k_2 = \frac{2\pi f^s \eta^s \gamma_T^2}{R^s}$ $\quad k_2 = 0$ $\quad k_3 = 0$

TABLE 3: Loop equations.

Loop Diagram:

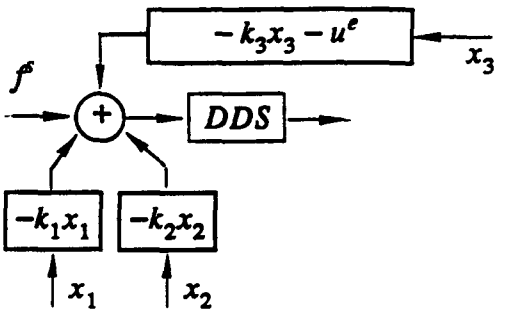

Feedback Strategy:

$$u = -k_1x_1 - k_2x_2 - k_3x_3 - u^e$$

Coefficients of the Characteristic Polynomial:

$$\bar{a}_0 = a_0 + a_1\epsilon + a_2\epsilon^2 + \epsilon^3 \qquad a_0 = a_{12}a_{23}b_{31}k_1 - a_{11}\tilde{a}_0$$

$$\bar{a}_1 = a_1 + 2\epsilon a_2 + 3\epsilon^2 \quad \text{and} \quad \tilde{a}_0 = a_{23}b_{31}k_2 - b_{31}a_{22}k_3 - a_{23}a_{32}$$

$$\bar{a}_2 = a_2 + 3\epsilon \qquad a_1 = \tilde{a}_0 - a_{11}(k_3b_{31} - a_{22})$$

$$a_2 = k_3b_{31} - (a_{11} + a_{22})$$

Stability Inequalities:

(i) $(\bar{a}_2\bar{a}_1 - \bar{a}_0) > 0$

(ii) $\bar{a}_2 > 0$

(iii) $\bar{a}_0 > 0$

Instability Boundaries for $\epsilon = 0$, $a_{11} = 0$, $a_{22} = 0$:

$$k_1 + 2\pi M k_2 = \frac{2\pi f^s}{v^s}k_3 \qquad k_1 = 0 \qquad k_3 = 0$$

TABLE 4: Loop equations.

Loop Diagram:

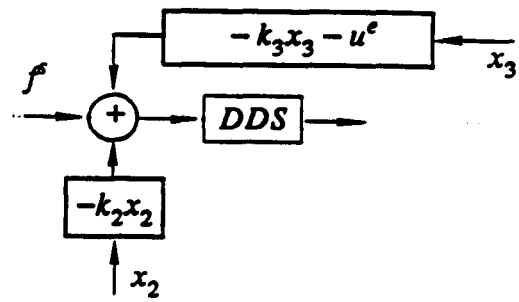

Feedback Strategy:

$u = -k_2x_2 - k_3x_3 - u^e$

Coefficients of the Characteristic Polynomial:

$\bar{a}_0 = a_0 + a_1\epsilon + \epsilon^2$ $\quad a_0 = a_{23}(k_2b_{31} - a_{32}) - a_{22}b_{31}k_3$

$\bar{a}_1 = a_1 + 2\epsilon$ and $a_1 = k_3b_{31} - a_{22}$

Stability Inequalities:

(i) $\bar{a}_1 > 0$

(ii) $\bar{a}_0 > 0$

Instability Boundaries for $\epsilon = 0$, $a_{11} = 0$, $a_{22} = 0$:

$k_2 = \frac{f^s\eta^s\gamma_T^2}{R^s}$ $\quad k_3 = 0$

TABLE 5: Loop equations.

Loop Diagram:

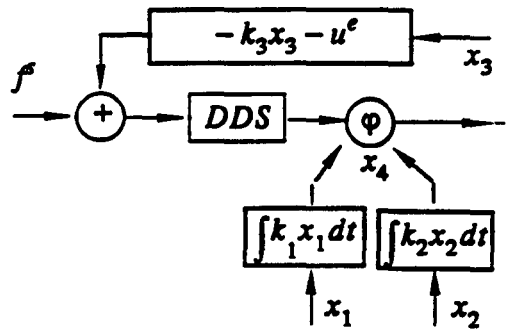

Feedback Strategy:

$u = -k_3x_3 - u^e$

$v = -k_1x_1 - k_2x_2$

Coefficients of the Characteristic Polynomial:

$$\bar{a}_0 = a_0 + \epsilon(a_1 + \epsilon a_2 + \epsilon^2 a_3 + \epsilon^3) \qquad a_0 = -a_{12}a_{23}b_{31}k_1k_3 + a_{11}a_{23}b_{31}k_2$$

$$\bar{a}_1 = a_1 + \epsilon(2a_2 + 3\epsilon a_3 + 4\epsilon^2) \qquad a_1 = (a_{11}a_{22} - a_{23}k_2)b_{31}k_3 + a_{11}a_{23}a_{32}$$

$$\bar{a}_2 = a_2 + 3\epsilon(a_3 + 2\epsilon) \quad \text{and} \quad a_2 = -k_3b_{31}(a_{11} + a_{22}) - a_{23}a_{32} + a_{11}a_{22}$$

$$\bar{a}_3 = a_3 + 4\epsilon \qquad a_3 = k_3b_{31} - (a_{11} + a_{22})$$

Stability Inequalities:

(i) $(\bar{a}_3\bar{a}_2 - \bar{a}_1)\bar{a}_1 - \bar{a}_3^2\bar{a}_0 > 0$

(ii) $(\bar{a}_3\bar{a}_2 - \bar{a}_1) > 0$

(iii) $\bar{a}_3 > 0$

(iv) $\bar{a}_0 > 0$

Instability Boundaries for $\epsilon = 0$, $a_{11} = 0$, $a_{22} = 0$:

$$k_1 = Pk_2^2 + Qk_2 \qquad k_2 = \frac{2\pi f^s\eta^s\gamma_T^2}{R^s} \qquad k_1 = 0 \qquad k_3 = 0$$

with $P = \frac{R^s c\nu^2}{2\pi h v^s(\eta^s\gamma_T^2)^2 k_3}$ $\qquad Q = -\frac{f c\nu^2}{h v^s\eta^s\gamma_T^2 k_3}$

Vertex of the parabola:

$$\left\{-\frac{\pi f^{s2}c\nu^2}{2hR^s v^s k_3}, \frac{\pi f^s\eta^s\gamma_T^2}{R^s}\right\}$$

TABLE 6: Loop equations.

Loop Diagram:

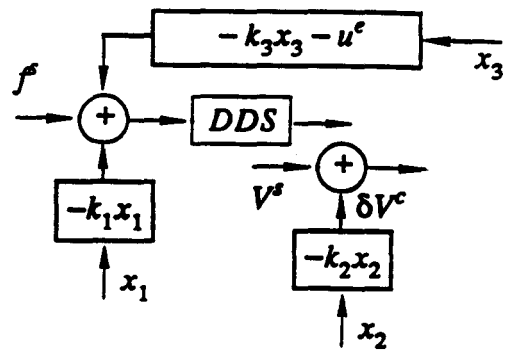

Feedback Strategy:

$u = -k_1x_1 - k_3x_3 - u^e$

$\omega = -k_2x_2$

Coefficients of the Characteristic Polynomial:

$$\bar{a}_0 = a_0 + a_1\epsilon + a_2\epsilon^2 + \epsilon^3 \qquad a_0 = a_{12}a_{23}b_{31}k_1 + a_{11}\tilde{a}_0$$

$$\bar{a}_1 = a_1 + 2\epsilon a_2 + 3\epsilon^2 \quad \text{and} \quad \tilde{a}_0 = \tilde{a}_{24}b_{31}k_2k_3 + b_{31}a_{22}k_3 + a_{23}a_{32}$$

$$\bar{a}_2 = a_2 + 3\epsilon \qquad a_1 = -\tilde{a}_0 + a_{11}(-k_3b_{31} + k_2\tilde{a}_{24} + a_{22})$$

$$a_2 = k_3b_{31} - (k_2\tilde{a}_{24} + a_{11} + a_{22})$$

Stability Inequalities:

(i) $(\bar{a}_2\bar{a}_1 - \bar{a}_0) > 0$

(ii) $\bar{a}_2 > 0$

(iii) $\bar{a}_0 > 0$

Instability Boundaries for $\epsilon = 0$, $a_{11} = 0$, $a_{22} = 0$:

$$k_1 = Pk_2^2 + Qk_2 + R \qquad k_1 = 0 \qquad k_2 = \frac{2\pi h\eta^s\gamma_T^2 k_3}{c\nu^2 \tan\phi_0^s}$$

with $P = \frac{R^s c\nu^2(\tan\phi_0^s)^2 k_3}{hv^s(\eta^s\gamma_T^2)^2}$ $\quad Q = -\frac{\tan\phi_0^s(fc\nu^2 + 2\pi R^s hk_3^2)}{hv^s\eta^s\gamma_T^2}$ $\quad R = \frac{2\pi f^s}{v^s}k_3$

Vertex of the parabola:

$$\left\{\left(\frac{2\pi f^s}{v^s}k_3 - \frac{(fc\nu^2 + 2\pi R^s hk_3^2)^2}{4hv^s R^s c\nu^2 k_3}\right), \left(\frac{(fc\nu^2 + 2\pi R^s hk_3^2)\eta^s\gamma_T^2}{2R^s c\nu^2 k_3 \tan\phi_0^s}\right)\right\}$$

TABLE 7: Loop Equations.

Loop Diagram:

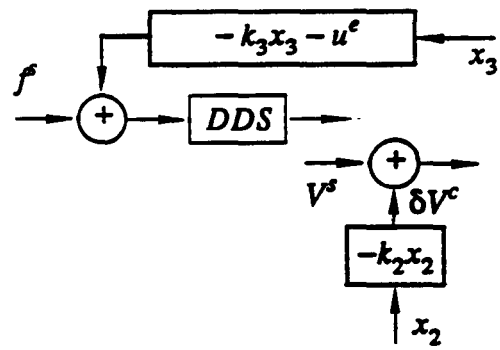

Feedback Strategy:

$u = -k_3x_3 - u^e$

$\omega = -k_2x_2$

Coefficients of the Characteristic Polynomial:

$\bar{a}_0 = a_0 + a_1\epsilon + \epsilon^2$ $\qquad a_0 = -(\tilde{a}_{24}b_{31}k_2k_3 + b_{31}a_{22}k_3 + a_{23}a_{32})$

$\bar{a}_1 = a_1 + 2\epsilon$ and $a_1 = k_3b_{31} - (k_2\tilde{a}_{24} + a_{22})$

Stability Inequalities:

(i) $\bar{a}_1 > 0$

(ii) $\bar{a}_0 > 0$

Instability Boundaries for $\epsilon = 0$, $a_{22} = 0$:

$$k_2 = \frac{2\pi h\eta^s\gamma_T^2 k_3}{c\nu^2 \tan\phi_0^s} \qquad k_2 = \frac{f^s\eta^s\gamma_T^2}{Rk_3\tan\phi_0^s}$$

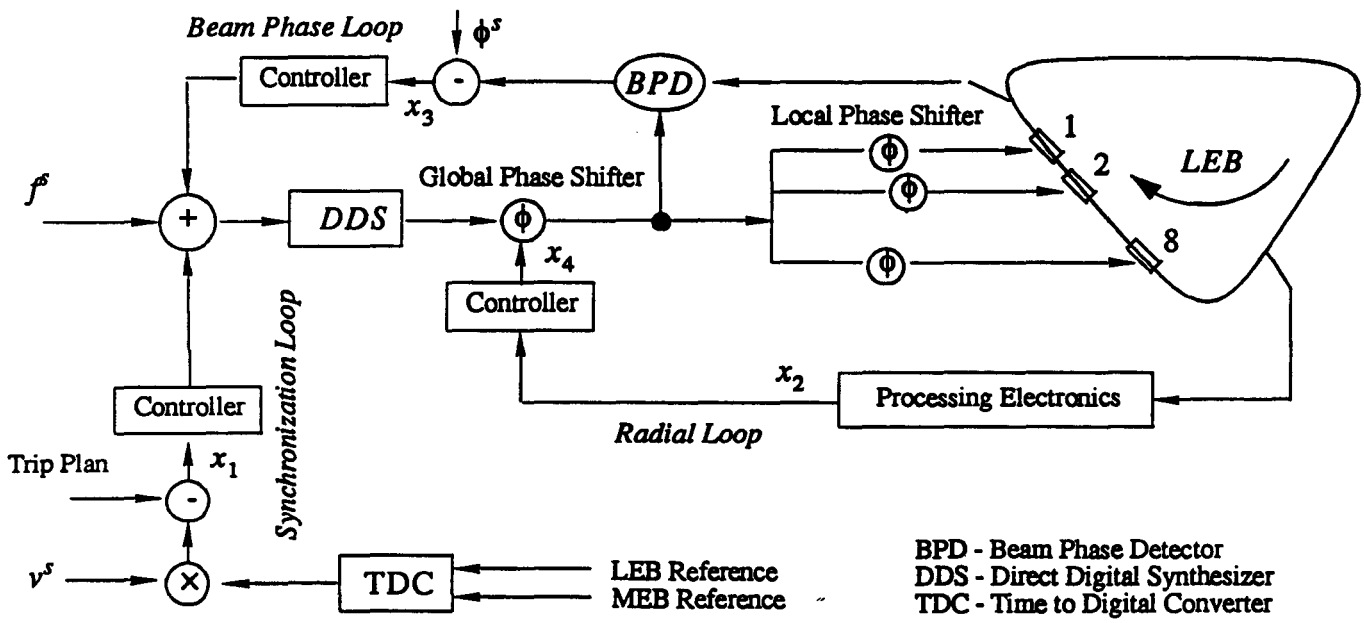

FIGURE 1. Schematic representation of the global beam control feedback loops for the LEB.

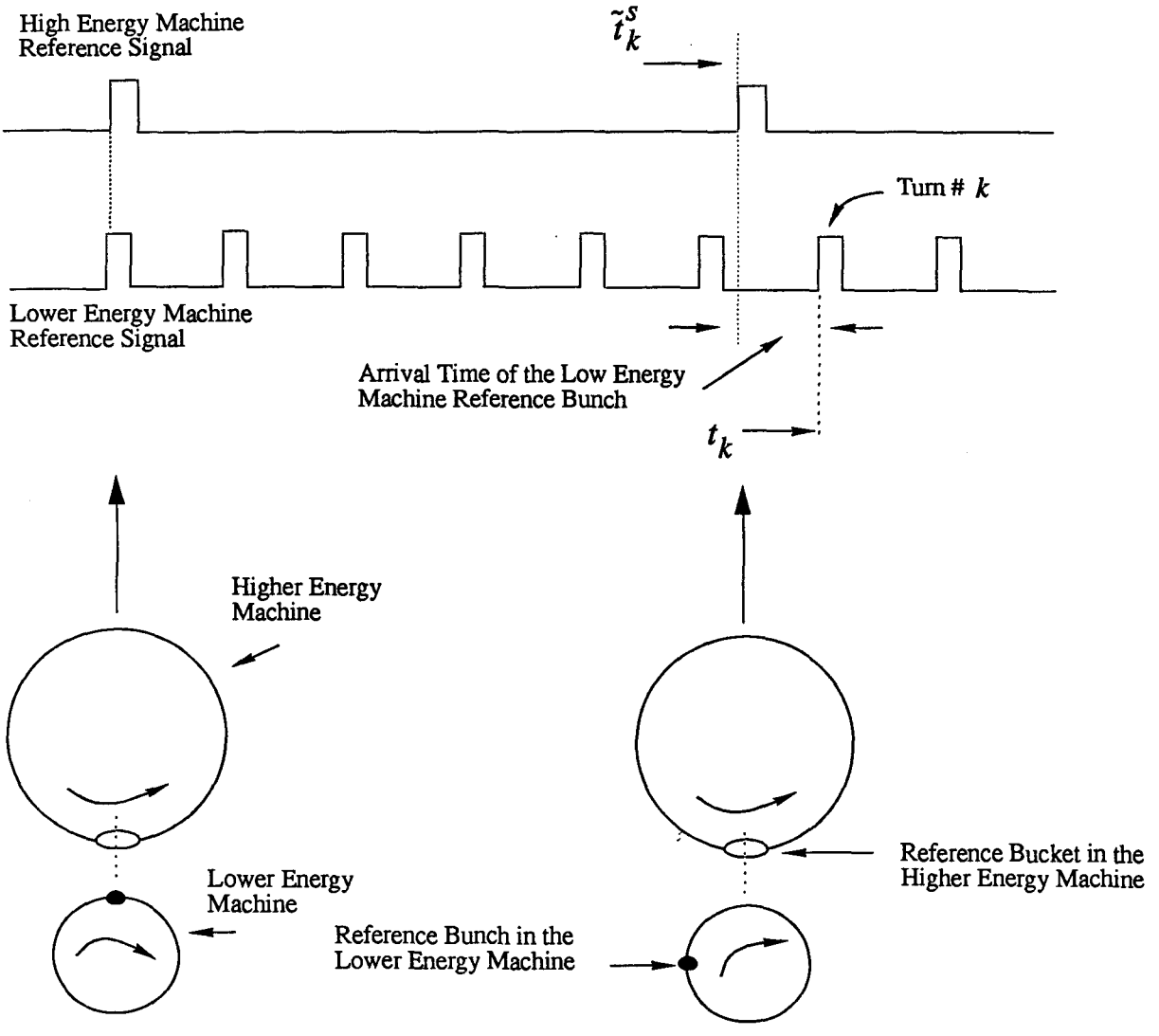

FIGURE 2. Conceptual diagram showing the arrival time of a reference bunch in the Lower-Energy Machine.

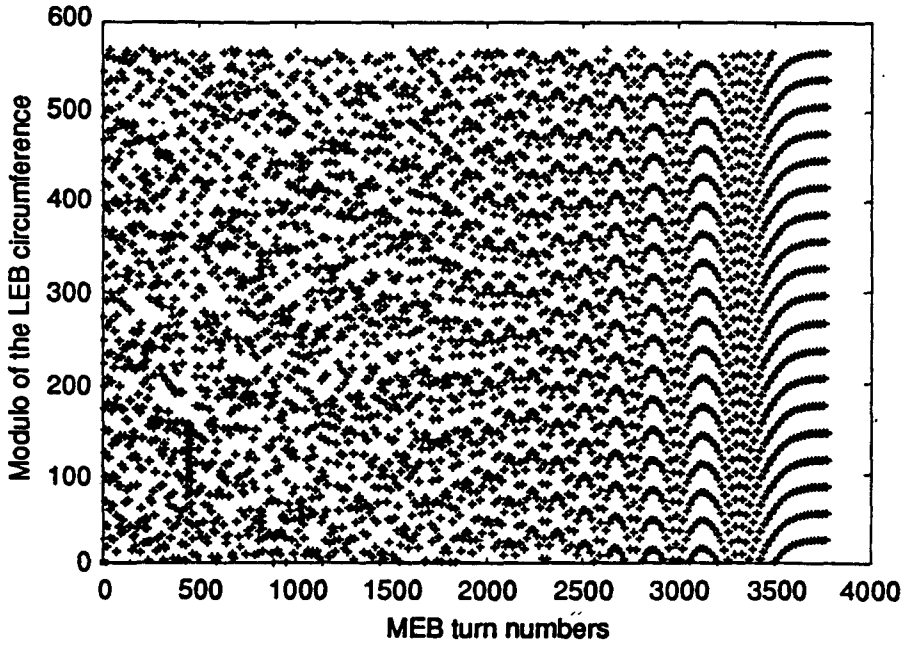

FIGURE 3. LEB trip-plan.

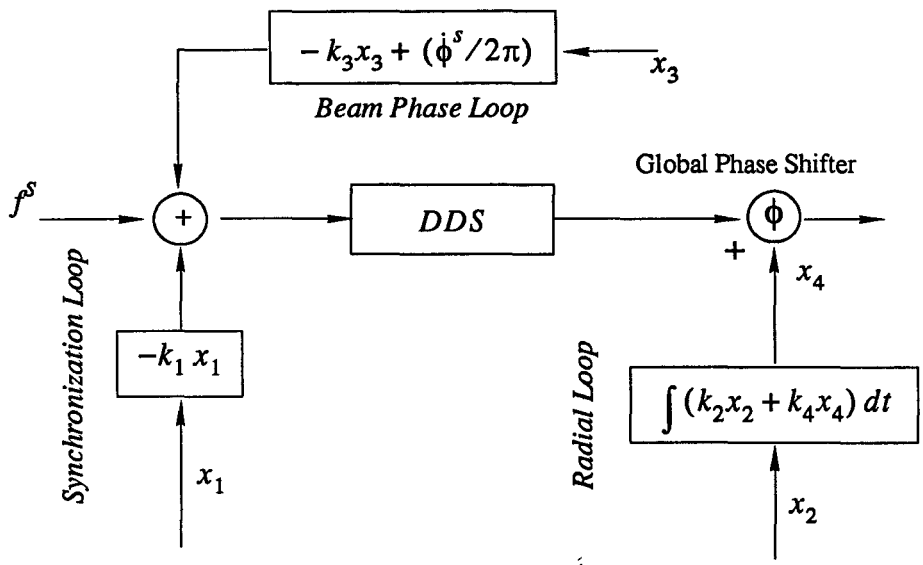

FIGURE 4. Schematic loop diagram of Fig. 1.

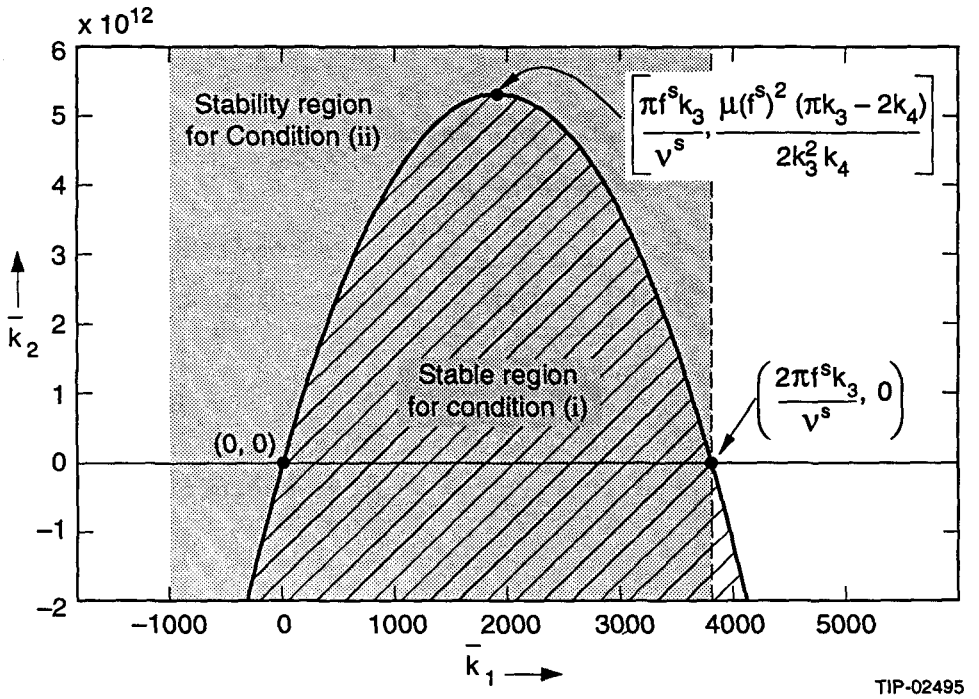

FIGURE 5. Stability region for conditions (i) and (ii) at 1 ms.

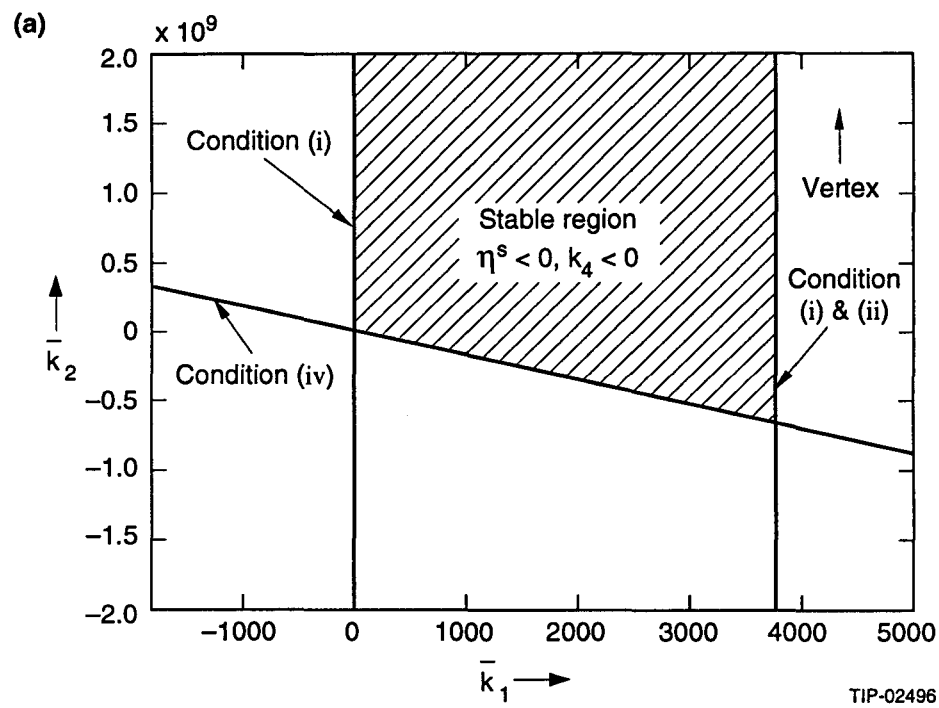

FIGURE 6(a). Combined stability region for Fig. 1 at 1 ms when $k_3 = 3000$, $k_4 = -20$.

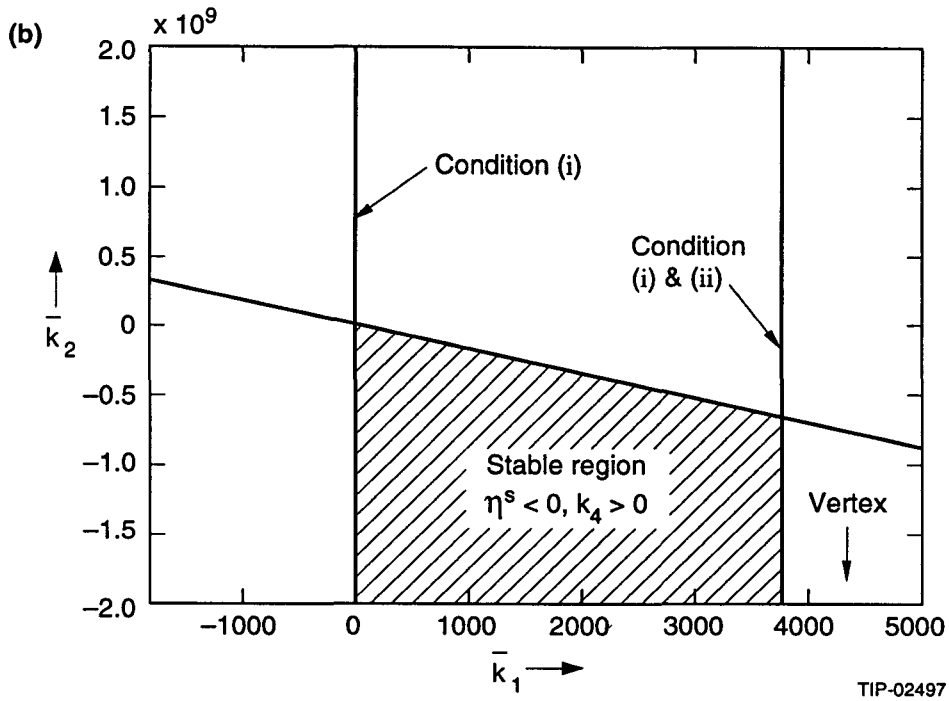

FIGURE 6(b). Combined stability region for Fig. 1 at 1 ms when $k_3 = 3000$, $k_4 = 20$.

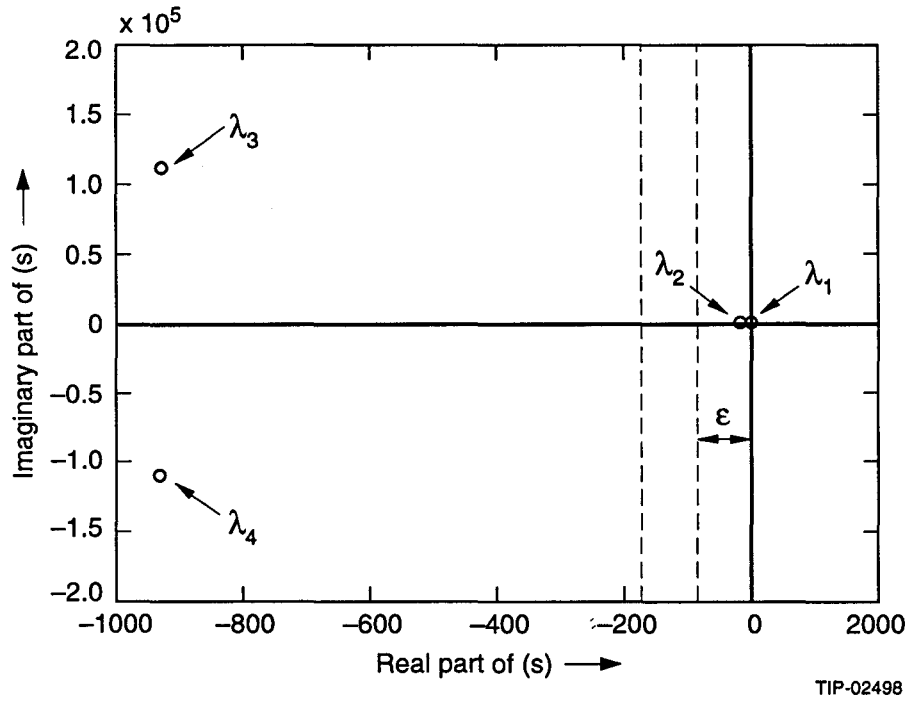

FIGURE 7. Eigen value locations at 1 ms for $k_1 = 25$, $k_2 = 5000$, $k_3 = 3000$ and $k_4 = -20$.

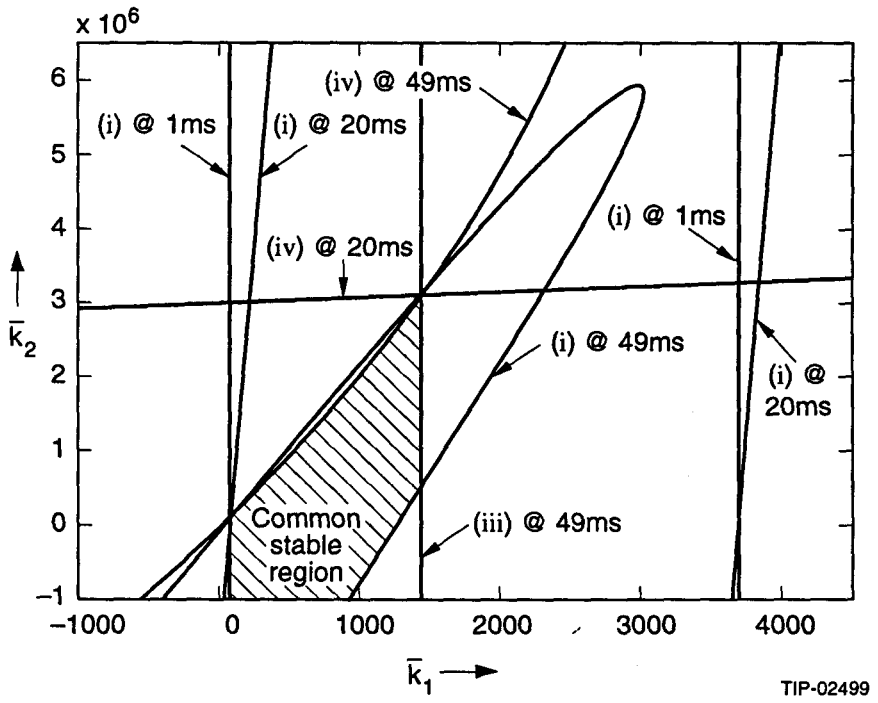

FIGURE 8. Common stability region for LEB when $k_3 = 3000$ and $\epsilon = -150$.

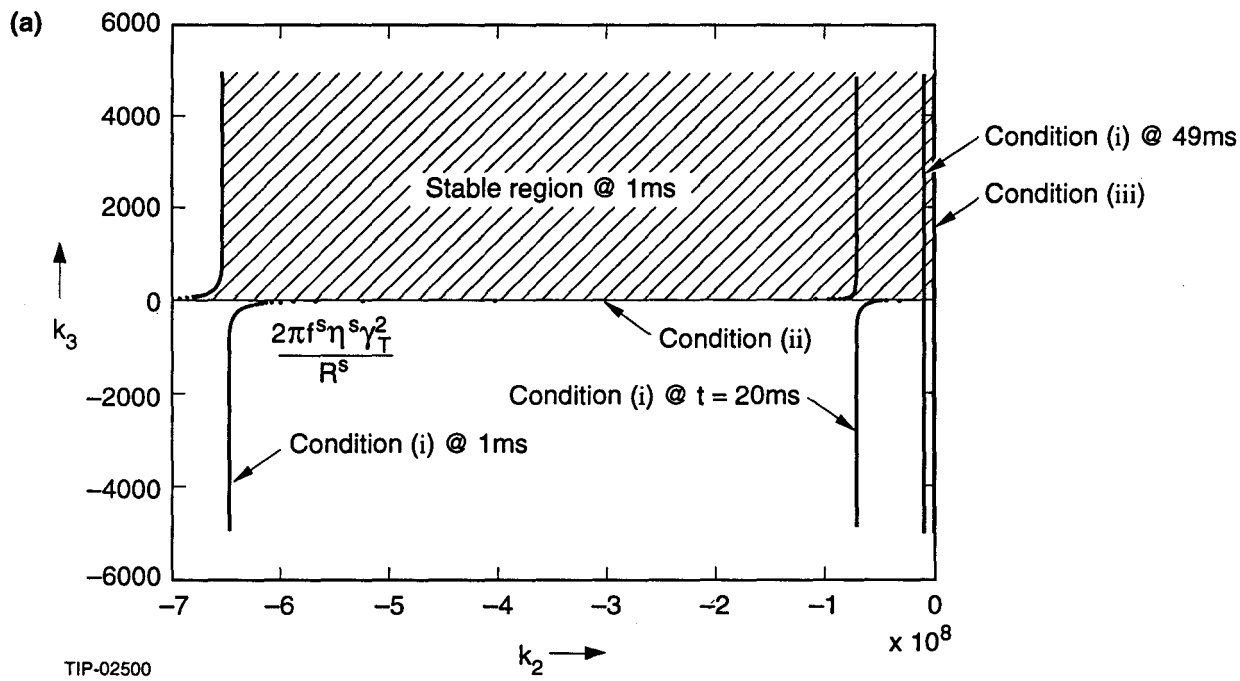

FIGURE 9(a). Stability diagram in k_2–k_3 space for Tab. 2 when $\epsilon = 0$.

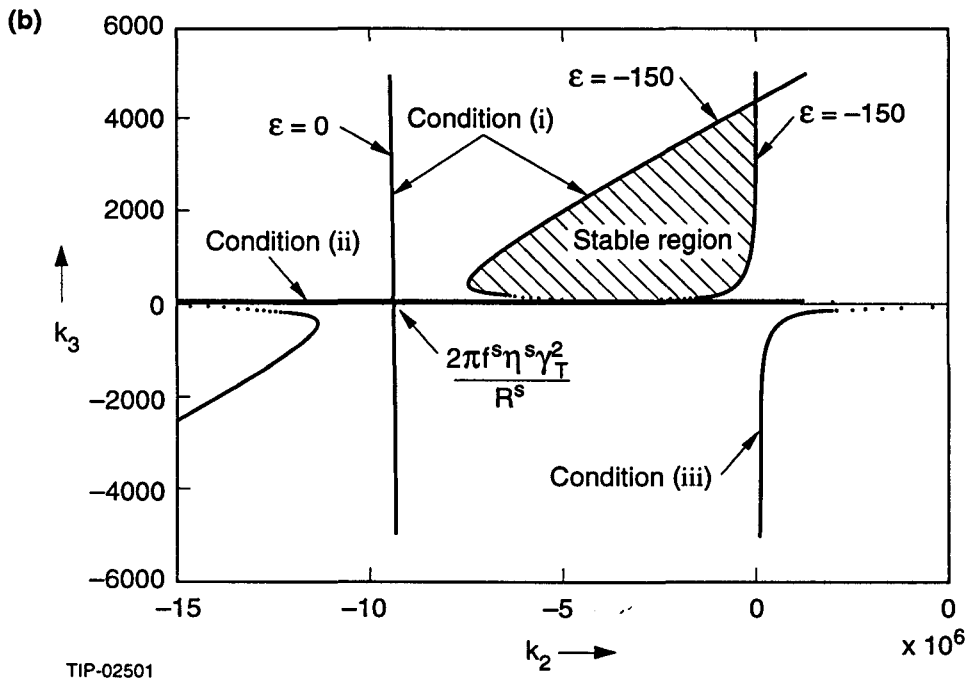

FIGURE 9(b). Stability diagram in k_2–k_3 space for Tab. 2 at 49 ms.

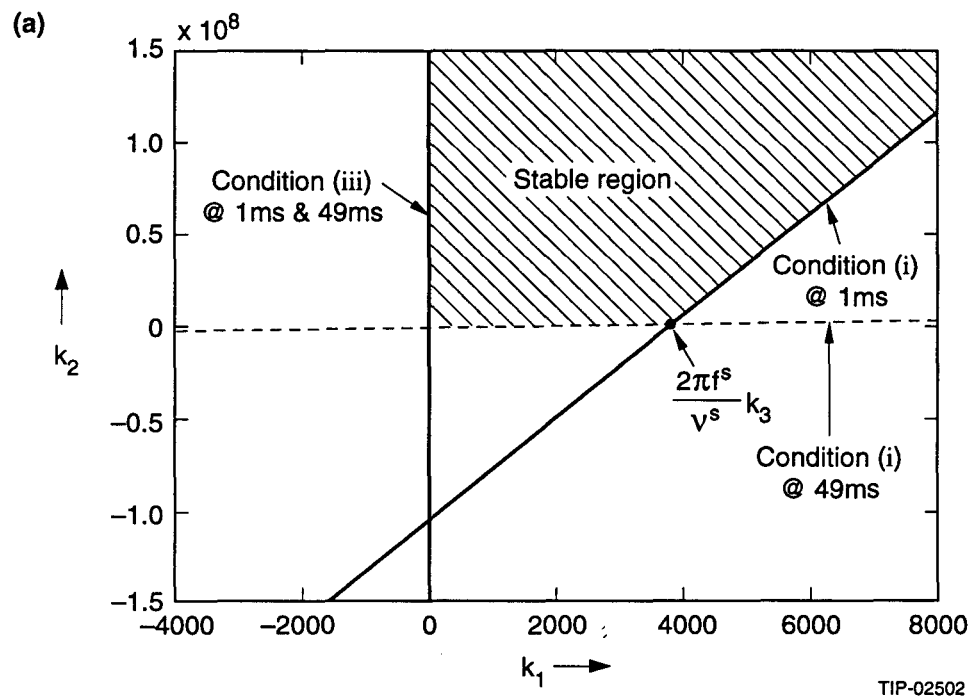

FIGURE 10(a). Stability diagram in k_1–k_2 space for Tab. 3 when $k_3 = 3000$ and $\epsilon = 0$.

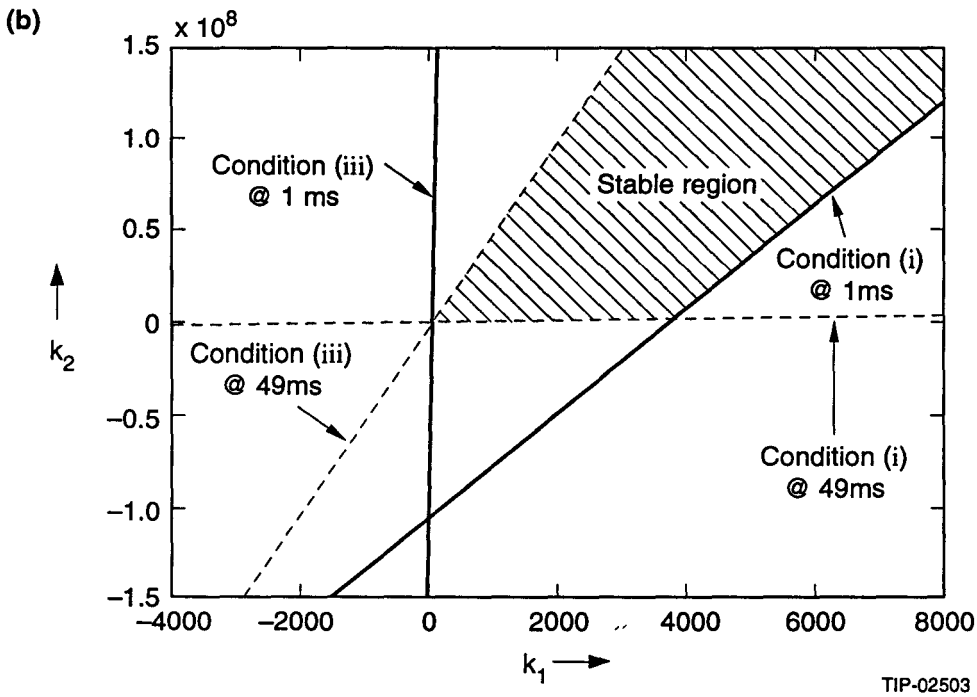

FIGURE 10(b). Stability diagram in k_1–k_2 space for Tab. 3 when $k_3 = 3000$ and $\epsilon = -150$.

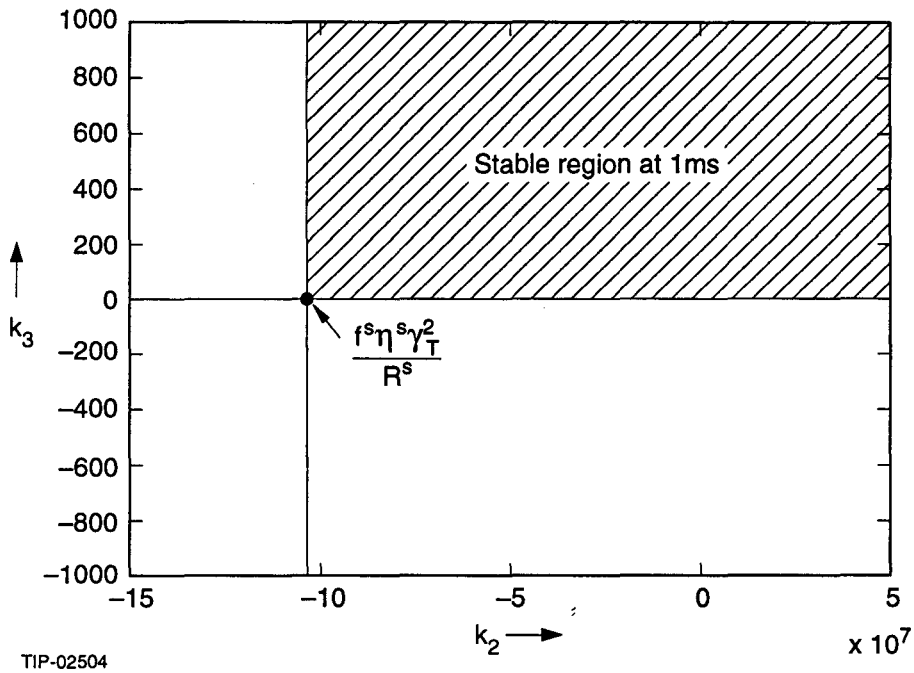

FIGURE 11. Stability diagram in k_3–k_2 space for Tab. 4 for $\epsilon = 0$ at 1 ms.

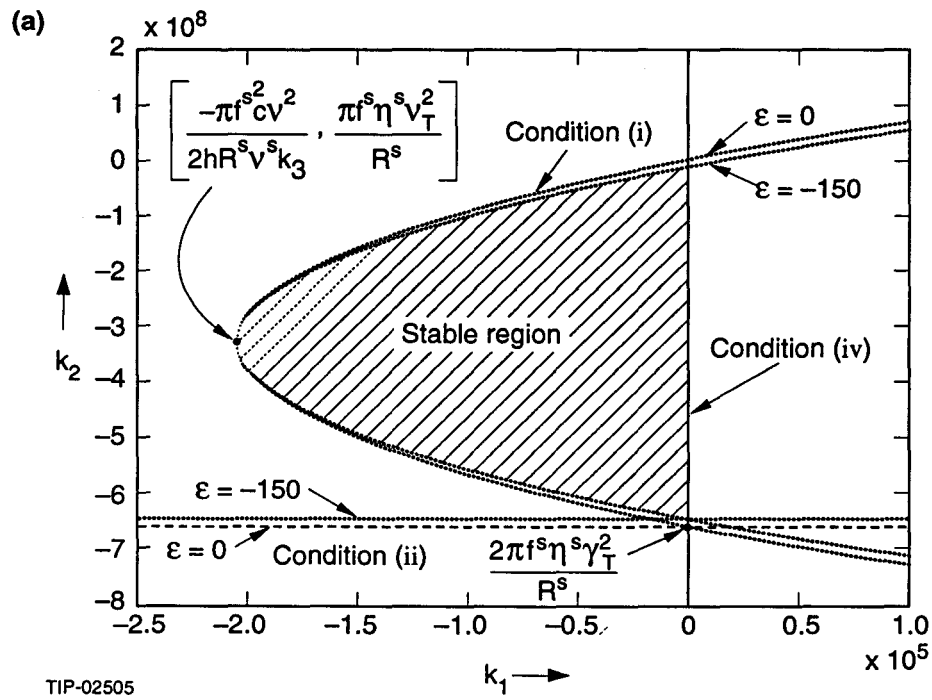

FIGURE 12(a). Stability region in k_1–k_2 space for Tab. 5 when $k_3 = 3000$ at 1 ms.

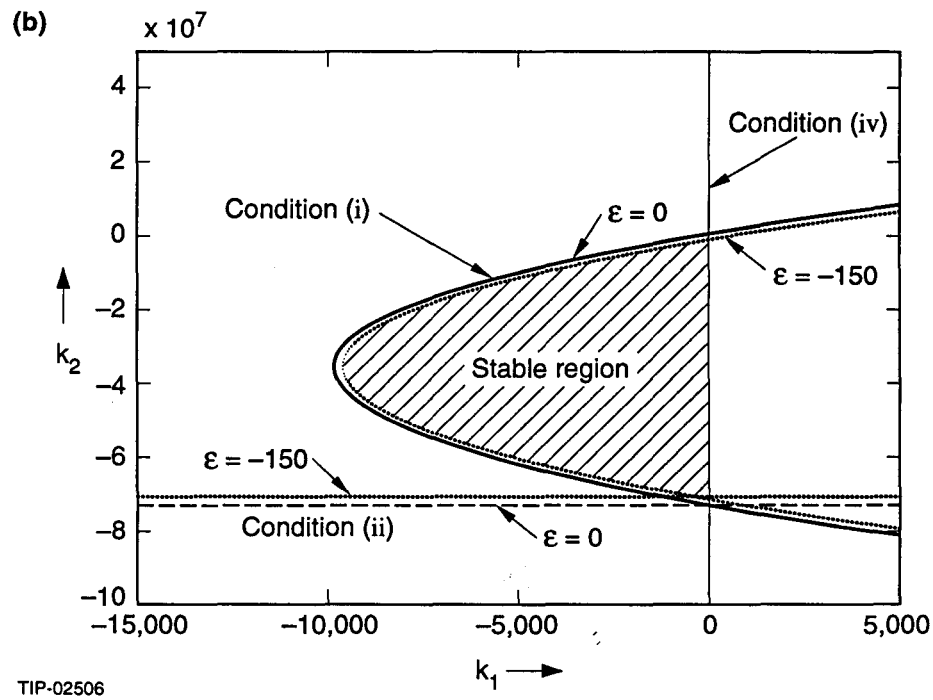

FIGURE 12(b). Stability region in k_1–k_2 space for Tab. 5 when $k_3 = 3000$ at 20 ms.

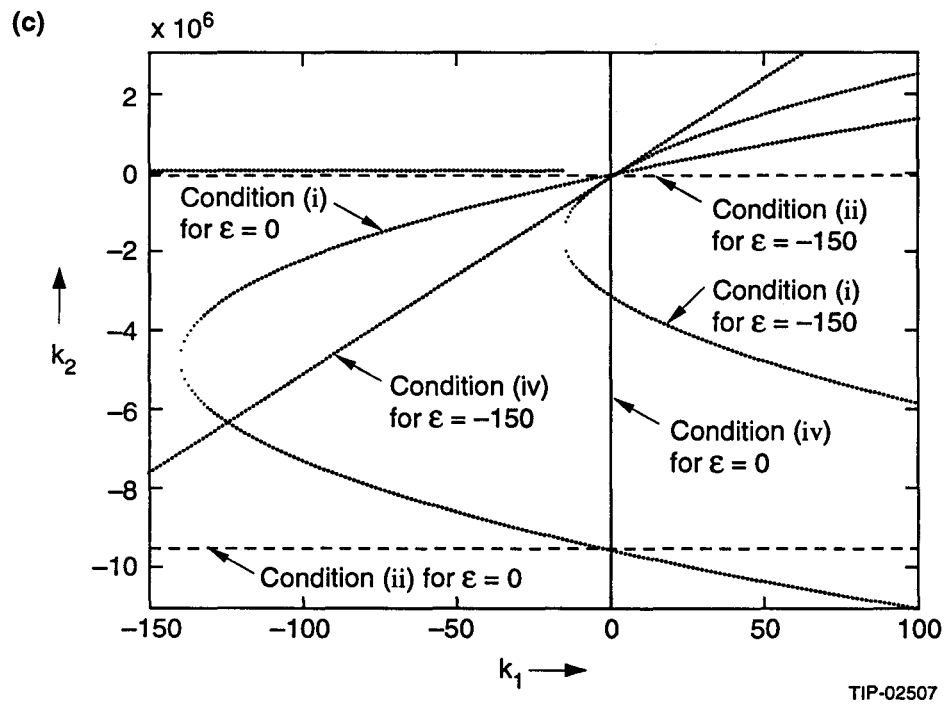

FIGURE 12(c). Stability region in k_1–k_2 space for Tab. 5 when $k_3 = 3000$ at 49 ms.

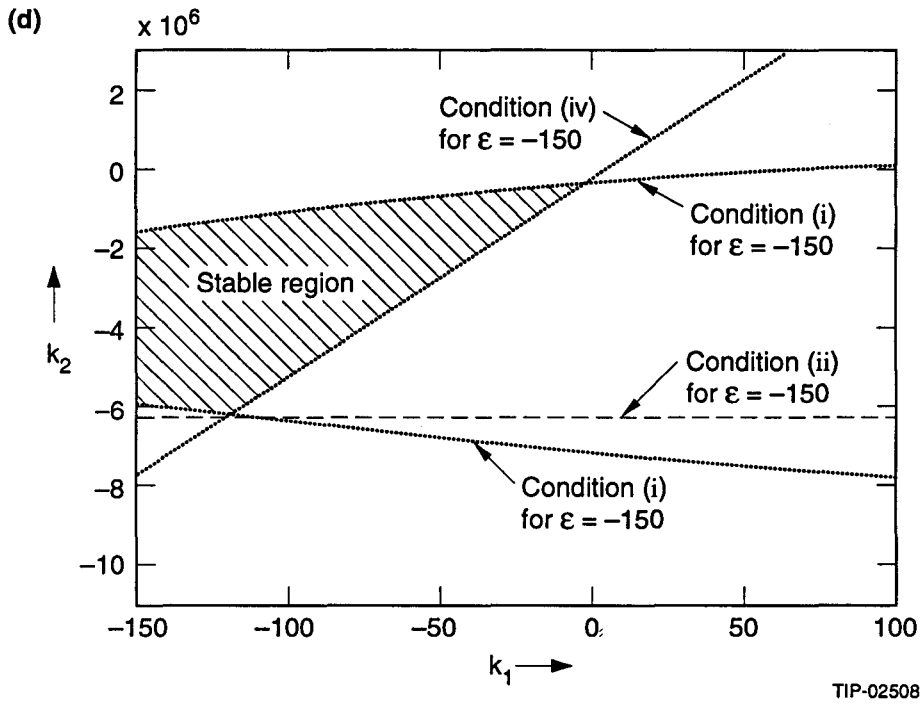

FIGURE 12(d). Stability region in k_1–k_2 space for Tab. 5 when $k_3 = 1000$ at 49 ms.

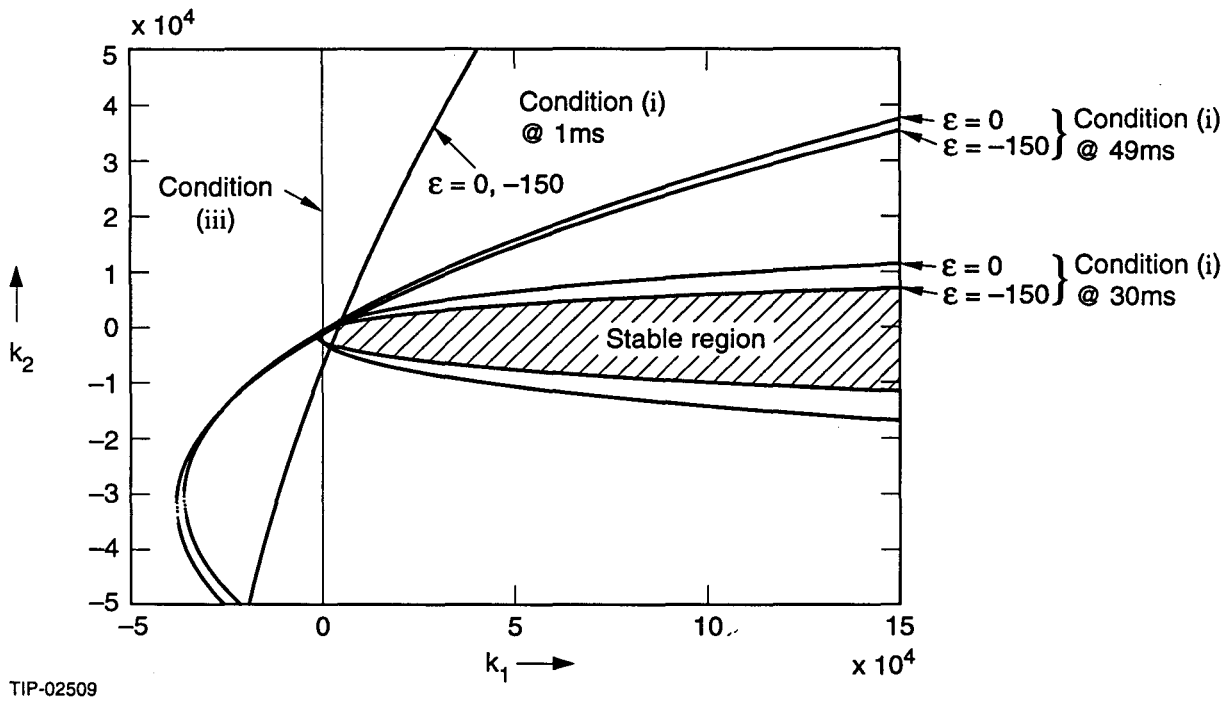

FIGURE 13. Stability region in k_1–k_2 space for Tab. 6 when $k_3 = 3000$.

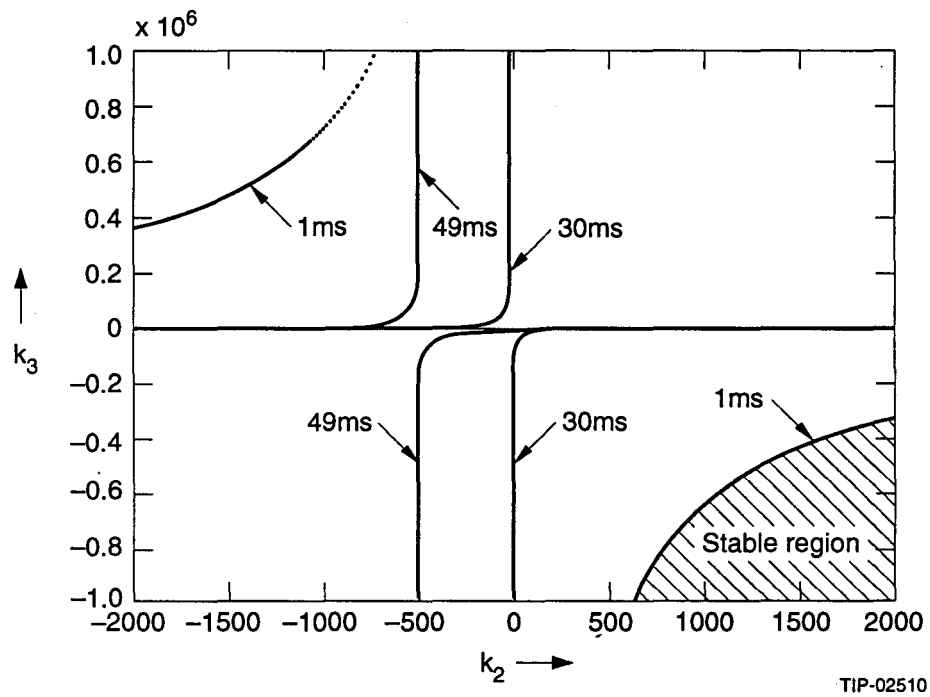

FIGURE 14. Stability region in k_2–k_3 space for Tab. 7 for $\epsilon = -150$.

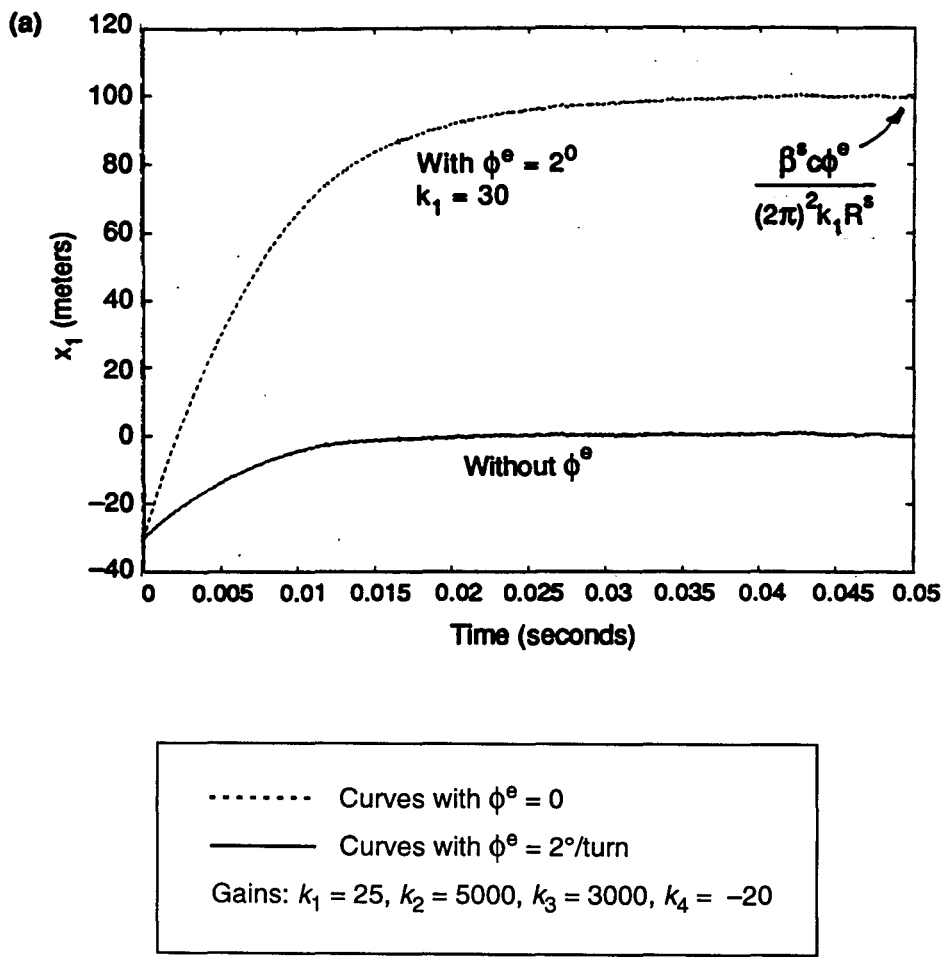

FIGURE 15(a). Synchronization phase error with respect to time.

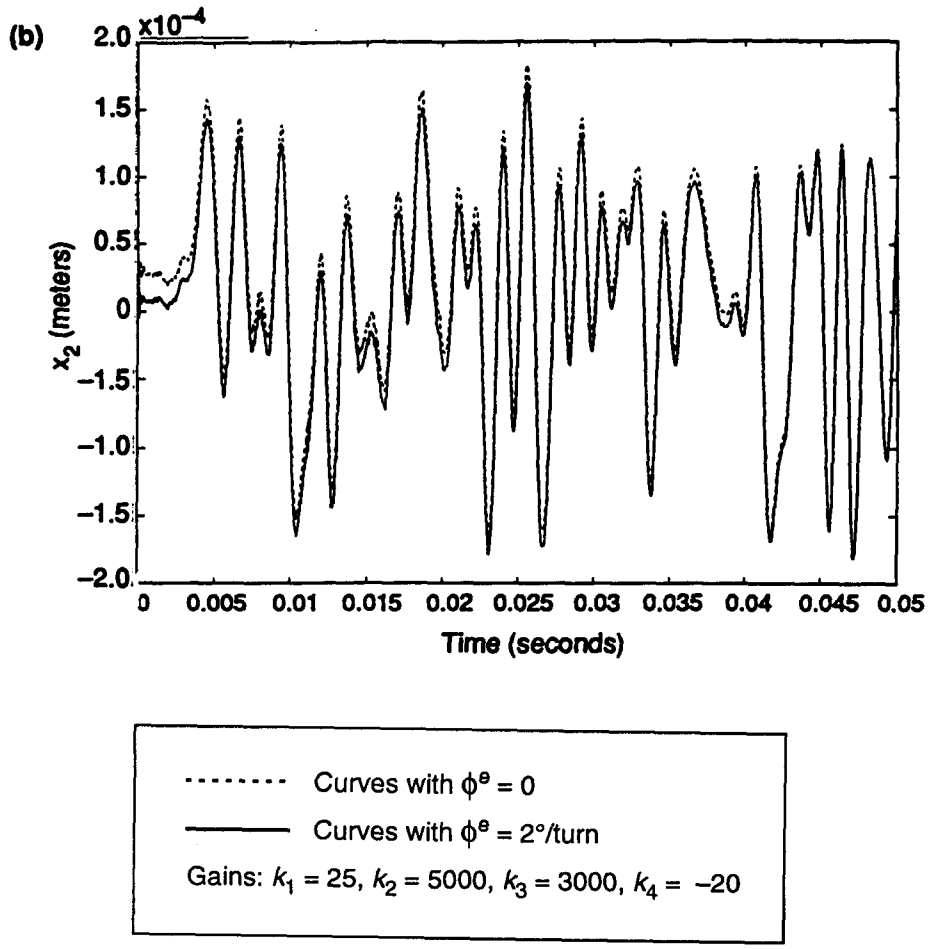

FIGURE 15(b). Radial orbit shift with respect to time.

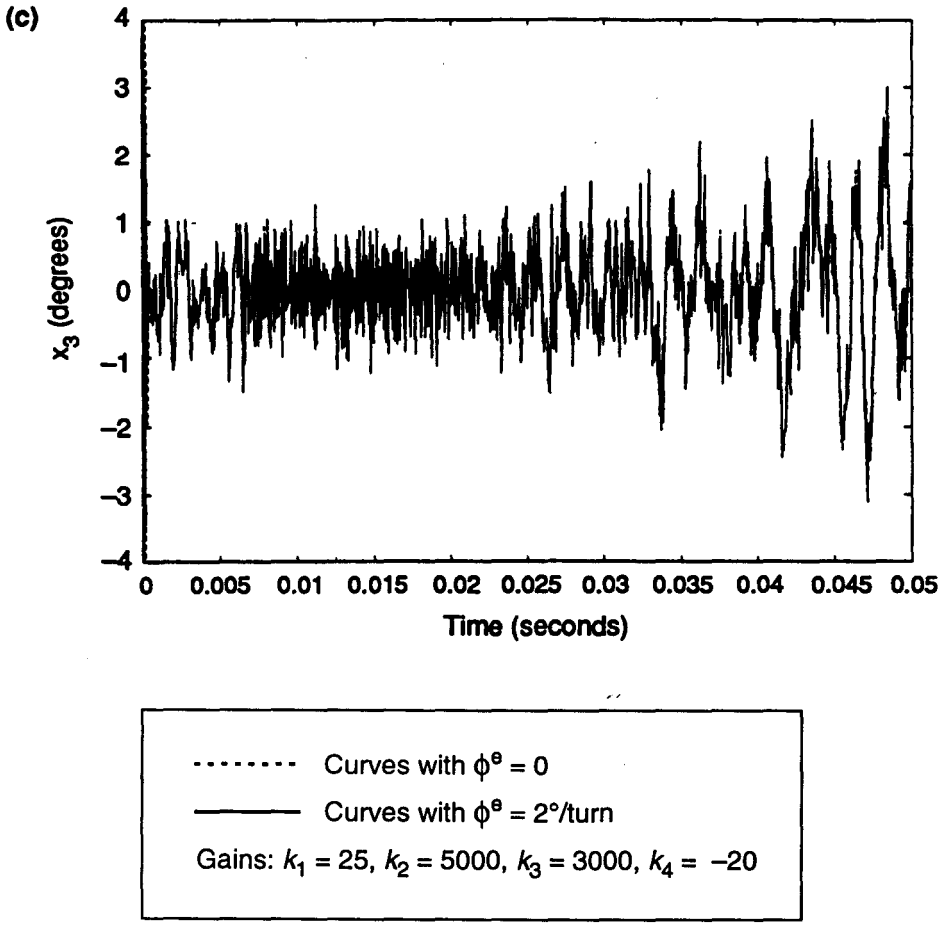

FIGURE 15(c). Beam phase error with respect to time.

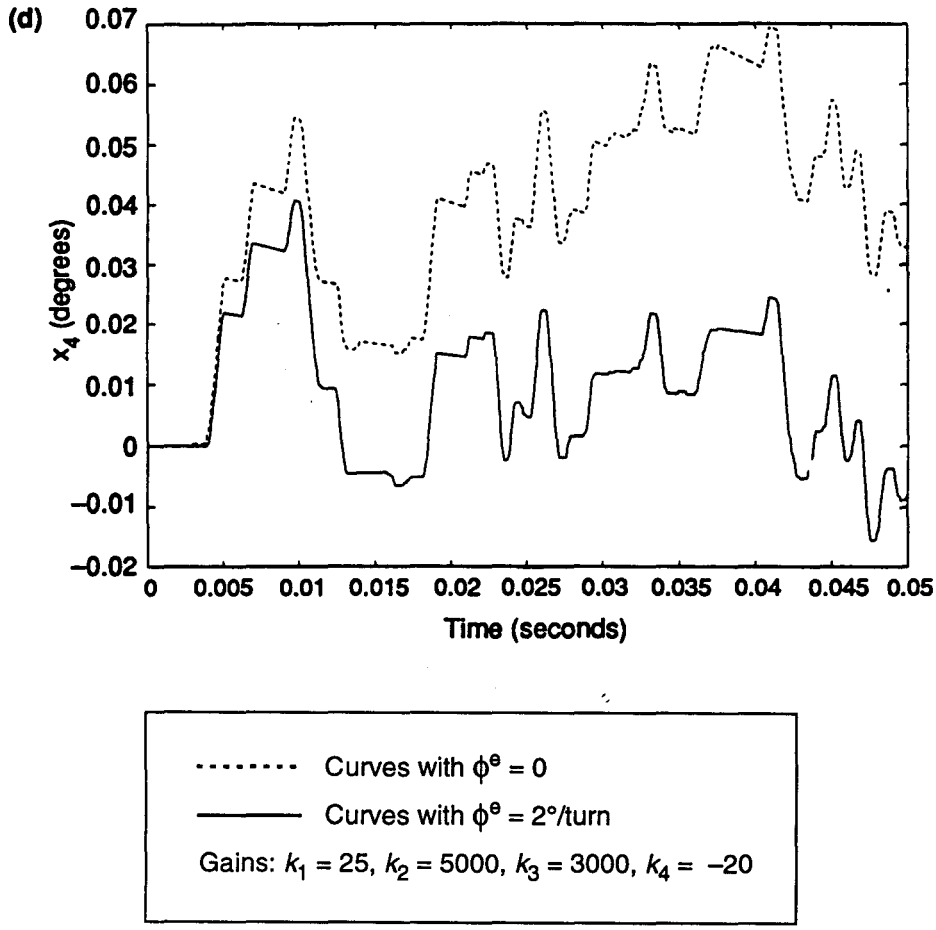

FIGURE 15(d). Global phase shift (control input) with respect to time.

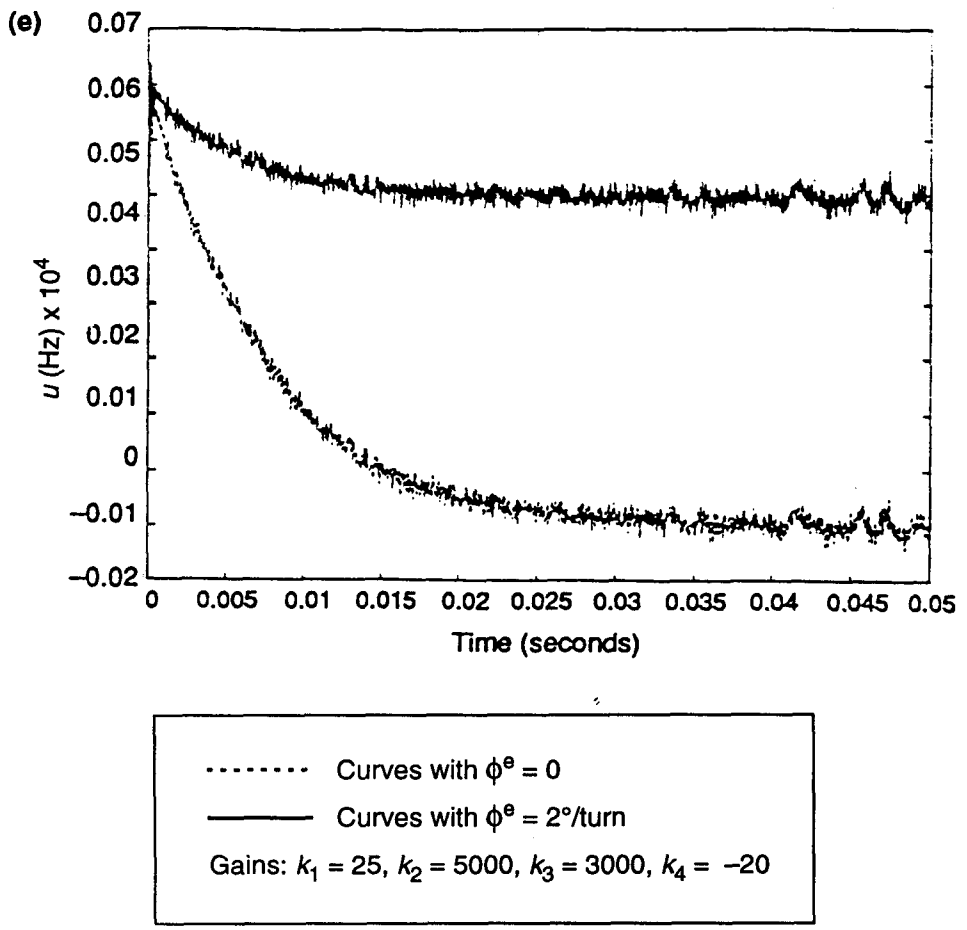

FIGURE 15(e). Frequency shift (control input) with respect to time.

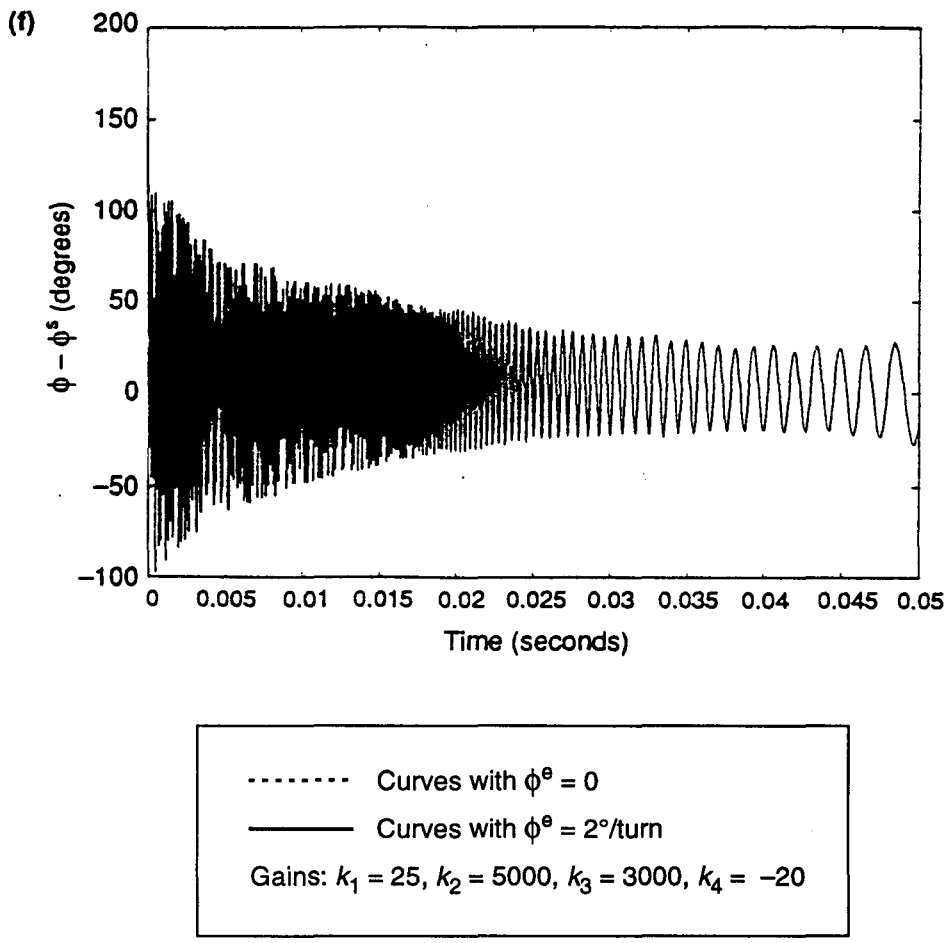

FIGURE 15(f). Phase difference of the offset particle with respect to time.

FIGURE CAPTIONS

FIGURE 1 Schematic representation of the global beam control feedback loops for the LEB.

FIGURE 2 Conceptual diagram showing the arrival time of a reference bunch in the Lower-Energy Machine.

FIGURE 3 LEB trip-plan.

FIGURE 4 Schematic loop diagram of Fig. 1.

FIGURE 5 Stability region for conditions (i) and (ii) at 1 ms.

FIGURE 6(a) Combined stability region for Fig. 1 at 1 ms when $k_3 = 3000$, $k_4 = -20$.

FIGURE 6(b) Combined stability region for Fig. 1 at 1 ms when $k_3 = 3000$, $k_4 = 20$.

FIGURE 7 Eigen value locations at 1 ms for $k_1 = 25$, $k_2 = 5000$, $k_3 = 3000$ and $k_4 = -20$.

FIGURE 8 Common stability region for LEB when $k_3 = 3000$ and $\epsilon = -150$.

FIGURE 9(a) Stability diagram in k_2–k_3 space for Tab. 2 when $\epsilon = 0$.

FIGURE 9(b) Stability diagram in k_2–k_3 space for Tab. 2 at 49 ms.

FIGURE 10(a) Stability diagram in k_1–k_2 space for Tab. 3 when $k_3 = 3000$ and $\epsilon = 0$.

FIGURE 10(b) Stability diagram in k_1–k_2 space for Tab. 3 when $k_3 = 3000$ and $\epsilon = -150$.

FIGURE 11 Stability diagram in k_3–k_2 space for Tab. 4 for $\epsilon = 0$ at 1 ms.

FIGURE 12(a) Stability region in k_1–k_2 space for Tab. 5 when $k_3 = 3000$ at 1 ms.

FIGURE 12(b) Stability region in k_1–k_2 space for Tab. 5 when $k_3 = 3000$ at 20 ms.

FIGURE 12(c) Stability region in k_1–k_2 space for Tab. 5 when $k_3 = 3000$ at 49 ms.

FIGURE 12(d) Stability region in k_1–k_2 space for Tab. 5 when $k_3 = 1000$ at 49 ms.

FIGURE 13 Stability region in k_1–k_2 space for Tab. 6 when $k_3 = 3000$.

FIGURE 14 Stability region in k_2–k_3 space for Tab. 7 for $\epsilon = -150$.

FIGURE 15(a) Synchronization phase error with respect to time.

FIGURE 15(b) Radial orbit shift with respect to time.

FIGURE 15(c) Beam phase error with respect to time.

FIGURE 15(d) Global phase shift (control input) with respect to time.

FIGURE 15(e) Frequency shift (control input) with respect to time.

FIGURE 15(f) Phase difference of the offset particle with respect to time.